

Continuous Unitary Designs for Universally Robust Quantum Control

Xiaodong Yang,^{1,2} Jiaqing Leng,¹ and Jun Li^{1,2,*}

¹*Institute of Quantum Precision Measurement, State Key Laboratory of Radio Frequency Heterogeneous Integration, College of Physics and Optoelectronic Engineering, Shenzhen University, Shenzhen 518060, China*

²*Quantum Science Center of Guangdong-Hong Kong-Macao Greater Bay Area (Guangdong), Shenzhen 518045, China*

Unitary designs are unitary ensembles that emulate Haar-random unitary statistics. They provide a vital tool for studying quantum randomness and have found broad applications in quantum technologies. However, existing research has focused on discrete ensembles, despite that many physical processes, such as in quantum chaos, thermalization, and control, naturally involve continuous ensembles generated from continuous time-evolution. Here we initial the study of continuous unitary designs, addressing fundamental questions about their construction and practical utility. For single-qubit system, we construct explicit unitary 1-design paths from spherical 2-design curves and Hopf fibration theory. For arbitrary dimensions, we develop two systematic construction frameworks, one based on topological bundle theory of the unitary group and the other based on the Heisenberg-Weyl group. On the practical front, our unitary design paths provide analytical solutions to universally robust quantum control. Simulations show they outperform conventional pulse techniques in mitigating arbitrary unknown static noises, demonstrating immediate utility for quantum engineering. Extending unitary designs to the continuous domain not only introduces powerful geometric and topological tools that complement conventional combinatorial and group-theoretic methods, but also enhances experimental feasibility over discrete counterparts which usually involve instantaneous pulses. As an outlook, we anticipate that this work will pave the way for using continuous unitary designs to explore complex quantum dynamics and devise quantum information protocols.

I. INTRODUCTION

This paper develops analytical methods for constructing *continuous unitary designs*. We define a continuous unitary t -design path as a unitary ensemble $\mathcal{E} = \{U(s)\}_{s \in [0,1]}$ that corresponds to a path in the unitary group and satisfies

$$\int_{[0,1]} f(U(s)) ds = \int f(U) dU \quad (1)$$

for any polynomial f up to degree t , where dU denotes the normalized Haar measure. These continuous designs generalize their discrete counterparts and enable important applications such as robust quantum control.

Randomness is fundamental to quantum processes and comprises a powerful resource for quantum technologies including algorithms, cryptography, and control. Harnessing this resource relies critically on the ability to implement random unitary operators. However, generating truly random unitaries by uniform sampling from the unitary group under Haar measure is inherently difficult, as most unitaries require exponential time to implement [1]. To address this difficulty, researchers introduced *unitary designs*, which are efficiently implementable unitary ensembles capable of emulating the statistical properties of true randomness [2–4]. Formally, an ensemble forms a unitary t -design if its first t statistical moments match the uniform Haar distribution [5]. Substantial research has explored generating such designs (exactly or approximately) via random quantum circuits [6–14] or other methods [15–19].

The capability to emulate Haar-random properties makes unitary designs exceptionally valuable both in theory and applications. Theoretically, they provide a powerful tool for studying random behaviors in many-body systems, advancing our understanding of fundamental phenomena including quantum chaos [20–22], thermalization [23, 24], entanglement evolution [25, 26], and complexity growth [27, 28]. Practically, unitary designs have become an indispensable tool in quantum information processing. For example, the single-qubit Pauli group forms a unitary 1-design that possesses universal decoupling property [29, 30]. The multiqubit Clifford group is a unitary 2-design that plays a vital role for quantum estimation, characterization, and benchmarking protocols [31–36]. Additionally, unitary designs have demonstrated utility in cryptography [37, 38], sensing [39], error correction [40], etc. Given their remarkable versatility, unitary designs continue to drive substantial efforts toward their constructions and applications [41–52].

Despite extensive research on unitary t -designs, the focus to date has predominantly been on discrete ensembles. However, many contexts naturally necessitate the consideration of continuous ensembles. A prominent example is universally robust control (URC), which aims to implement quantum gates resilient to arbitrary unknown noise. Recently, Ref. [53] established that URC corresponds precisely to the condition that the controlled evolution forms a unitary 1-design. The authors thence discretized the evolution and numerically optimized control pulses to make the discrete-time propagators satisfy this condition. However, numerical approaches face computational bottlenecks as system dimensionality grows exponentially with the number of qubits. Besides, the resulting solutions often lack physical interpretability. This

* lijunquantum@szu.edu.cn

raises the question: can we construct analytical continuous unitary 1-designs for URC? Indeed, experimentally implementable robust control pulses with simple analytical forms would be particularly valuable for practical applications. Beyond quantum control, in studying dynamical and statistical phenomena such as quantum chaos, thermalization, and ergodicity that arise in quantum many-body systems, it is also natural to consider continuous ensembles generated from continuous-time evolution [23, 42, 44].

A further motivation stems from recent developments in classical continuous spherical designs. As unitary designs trace their origin to spherical designs [54], a comparative study of their progress can be particularly fruitful. A spherical t -design is a finite subset of points on the d -sphere \mathbb{S}^d such that any polynomial of degree at most t has the same average on this set as on the entire sphere. Since their introduction in the late 1970s [55], spherical designs have been intensively studied, yet almost exclusively as discrete sets. Recently, mathematicians have paid attention to continuous versions [56–59]. Ref. [56] defines a *spherical t -design curve* as a closed curve $\gamma : [0, 1] \rightarrow \mathbb{S}^d$ of arc length $\ell(\gamma)$ satisfying $\frac{1}{\ell(\gamma)} \int_{\gamma} f = \int_{\mathbb{S}^d} f$ for all polynomials f in $d + 1$ variables of degree at most t . The fundamental question is hence how to construct curves with such design properties. This leads to novel construction methods for spherical designs, such as approaches based on Hopf fibration [58, 59]. Given the close relationship between unitary and spherical designs, it is natural and interesting to extend these concepts and methodologies to the study of continuous unitary designs.

Motivated by both the demand in quantum applications and the advances in classical spherical design curves, we initiate the study of continuous unitary designs. In this work, we focus on two fundamental aspects: construction and application. First, how to analytically construct unitary 1-design paths, as defined in Eq. (1)? A natural approach is to find a continuous path that connects a discrete unitary 1-design set, while ensuring the path itself also forms a design [60]. However, this turns out to be more challenging than it initially appears, especially in high-dimensional spaces. Our core idea leverages the profound connection between unitary designs and spherical designs. For a two-level system, the well-known equivalence between the manifold $\text{SU}(2)$ and the 3-sphere \mathbb{S}^3 permits the direct conversion of a spherical 2-design curve into a unitary 1-design path. However, this correspondence does not extend directly to higher dimensions since $\text{SU}(d)$ is not isomorphic to a sphere for $d > 2$. Despite this, we can exploit the fiber bundle structure of $\text{SU}(d)$, which is based over odd-dimensional spheres [61, 62]. This enables us to employ a lifting technique developed from [58, 59] to construct continuous unitary designs for arbitrary dimension d .

Second, regarding practical utility, continuous unitary design is of significance for tackling the noise challenge in near-term quantum technologies—specifically, the prob-

lem of URC as introduced earlier. In current quantum devices, noise is unavoidable and often arises from multiple concurrent sources [63–65]. As systems scale up, fully characterizing all the noise components in the exponentially large Liouvillian space becomes increasingly difficult [35]. Robust control aims to achieve high-fidelity gates while suppressing the noise effects without requiring full noise characterization [66]. However, widely used robust control techniques such as dynamical decoupling [60, 67, 68], composite pulses [69–72], and geometric evolution optimization [73–77], are usually limited to mitigating noise along specific directions. There is thus a need to develop URC methods applicable to arbitrary noise orientations and arbitrary target gates [53, 78, 79]. Our continuous unitary design framework can generate analytic solutions for URC. Numerical simulations confirm that the resulting analytic pulses enable robust single-qubit identity and dynamical decoupling operations, offering immunity to arbitrary static noise while outperforming conventional composite pulses and dynamical decoupling sequences. These pulses also exhibit robustness against multi-axis, slowly varying, and time-correlated noise. This work establishes a foundation for the analytical design of URCs, opening a viable route toward reliable quantum control in realistic, noisy experimental settings.

Our main results are summarized as follows:

- (1) For a single-qubit system, we construct a closed continuous unitary 1-design path of length $\sqrt{5}\pi$, defined by

$$U(\theta) = R_{\mathbf{n}_1}(\theta)R_{\mathbf{n}_2}(2\theta), \quad (2)$$

where $\theta = 2\pi s$ with $s \in [0, 1]$, \mathbf{n}_1 and \mathbf{n}_2 are any pair of mutually perpendicular rotational axes. This path is generalizable, allowing its endpoint to be reconfigured to match an arbitrary target operator. As an example, a valid unitary 1-design path yielding a π rotation about the z -axis is

$$U(\theta(s)) = R_z(\theta(s))R_y(2\theta(s)), \quad (3)$$

where $\theta(s) : [0, 1] \rightarrow [0, 3\pi]$ is a continuous piecewise-linear function:

$$\theta(s) = \begin{cases} 4\pi s, & s \in [0, 1/4], \\ 2\pi s + \pi/2, & s \in [1/4, 3/4], \\ 4\pi s - \pi, & s \in [3/4, 1]. \end{cases}$$

A notable feature of the path $U(\theta)$ in Eq. (2) is that any finite equiangular sampling of $N \geq 4$ points $\{\theta_k = 2\pi k/N\}_{k=0}^{N-1}$ of the path still forms a unitary 1-design. This property is advantageous for experimental pulse controls with finite time resolution. In contrast, Eq. (3) does not possess this property.

- (2) For higher-dimensional systems, we present two general construction methods. The first leverages the topological structure of the $\text{SU}(d)$ group. Using

the fiber bundle $\mathbb{SU}(d-1) \hookrightarrow \mathbb{SU}(d) \rightarrow \mathbb{S}^{2d-1}$, we develop an inductive procedure to construct a unitary 1-design path in $\mathbb{SU}(d)$ from a corresponding path in $\mathbb{SU}(d-1)$ and a spherical 2-design curve on \mathbb{S}^{2d-1} . The second method is based on the a discrete unitary 1-design Heisenberg-Weyl group. We construct a path that connects its elements and simultaneously forms a unitary 1-design.

(3) We derive analytic URC pulse from the constructed unitary 1-design paths and verify their performance through numerical simulations. As an illustrative example, we focus primarily on single-qubit control based on the path specified in Eq. (2). It is important to emphasize that this equation does not represent applying two separate quantum gates, but rather defines a controlled evolution path. Our objective is to inversely determine a corresponding control pulse that generates this path exactly. Using inverse engineering, we obtain the explicit pulse form as follows:

$$\mathbf{u}(t) = \frac{\Omega}{\sqrt{5}} \left(-2 \sin\left(\frac{\Omega}{\sqrt{5}}t\right), 2 \cos\left(\frac{\Omega}{\sqrt{5}}t\right), 1 \right),$$

where $t \in [0, 2\pi\sqrt{5}/\Omega]$, and Ω is the maximum Rabi power that is allowed under experimental constraints. We compared its performance with conventional composite pulses like CORPSE and BB1, and found that URC can resist static or slowly varying noise from any direction. Furthermore, repeated applications of this URC pulse form a dynamical decoupling sequence applicable for quantum memory. Our simulations demonstrate that this sequence outperforms conventional sequences like CPMG and XY4 in preserving quantum memory under static noise of unknown amplitude acting along arbitrary spatial directions.

II. PRELIMINARIES

This section covers the basic notations and notions, and some known results that serve as the basis for this work.

A. Unitary Design

Let $\mathcal{H} \cong \mathbb{C}^d$ denote the d -dimensional Hilbert space and $\mathbb{U}(d)$ the group of unitary operators. A unitary t -design can be characterized through t -fold quantum twirling channels [35]. For a finite ensemble $\mathcal{E} = \{U_k\}_{k=1}^K \subset \mathbb{U}(d)$ with uniform weights, the t -fold twirling channel $\Phi_{\mathcal{E}}^{(t)}$ acts on any linear operator A of the t -fold Hilbert space $\mathcal{H}^{\otimes t}$ as

$$\Phi_{\mathcal{E}}^{(t)}(A) = \frac{1}{K} \sum_{k=1}^K U_k^{\otimes t} A (U_k^{\otimes t})^{\dagger}.$$

This definition can be extended to continuous ensembles by replacing the summation with integration. Let $\Phi_{\text{Haar}}^{(t)}$ denote the t -fold Haar-random twirling channel for $\mathbb{U}(d)$ with normalized Haar measure, then \mathcal{E} forms a unitary t -design if and only if

$$\Phi_{\mathcal{E}}^{(t)}(A) = \Phi_{\text{Haar}}^{(t)}(A)$$

for all A . This formulation establishes statistical indistinguishability of \mathcal{E} from Haar unitaries up to t th moment. The definition can also be expressed in terms of Pauli operators, which form a complete operator basis. Concretely, \mathcal{E} constitutes a unitary t -design iff $\Phi_{\mathcal{E}}^{(t)}(P) = \Phi_{\text{Haar}}^{(t)}(P)$ for all $P \in \{I, X, Y, Z\}^{\otimes t}$, where X , Y , and Z denote the Pauli operators σ_x , σ_y , and σ_z , respectively, and I represents the identity matrix. For $t = 1$, the Haar ensemble channel corresponds to a depolarizing map:

$$\Phi_{\mathcal{E}}^{(1)}(\rho) = \int_{\mathbb{U}(d)} U \rho U^{\dagger} dU = \frac{\text{Tr}(\rho)}{d} I,$$

for any Hermitian operator ρ . Therefore, an ensemble forms a unitary 1-design iff it averages every traceless Pauli operator to zero.

The unitary design property is invariant under global phase transformations. That is, if $\{U_k\}$ forms a unitary t -design, then so does $\{e^{i\theta_k} U_k\}$ for any choice of phases θ_k . Since the elements of the special unitary group $\mathbb{SU}(d)$ differ from those of $\mathbb{U}(d)$ only by global phases, we restrict to $\mathbb{SU}(d)$ in this work without loss of generality. Furthermore, a unitary t -design is automatically a t' -design for $t' < t$, and remains invariant under left multiplication, right multiplication, or conjugation by any fixed $V \in \mathbb{SU}(d)$, reflecting Haar measure invariance.

The N -qubit Pauli group defined by $\mathcal{P}_N := \{\pm 1, \pm i\} \cdot \{I, X, Y, Z\}^{\otimes N}$ is known for being a unitary 1-design. For example, the set $\{I, iX, iY, iZ\}$ is a unitary 1-design in $\mathbb{SU}(2)$. The N -qubit Clifford group, defined as the normalizer of the Pauli group, constitutes a unitary 2-design and is known to be a 3-design but not a 4-design [80].

A powerful diagnostic tool for verifying unitary design properties is the t th frame potential [20], defined as:

$$\mathcal{F}_{\mathcal{E}}^{(t)} = \frac{1}{K^2} \sum_{k,j=1}^K \left| \text{Tr}(U_k^{\dagger} U_j) \right|^{2t}. \quad (4)$$

This quantity provides a lower bound for the Haar frame potential $\mathcal{F}^{(t)}(\mathcal{E}) \geq \mathcal{F}_{\text{Haar}}^{(t)} = t!$, with equality iff the ensemble forms a t -design. In particular, $\mathcal{F}^{(1)} = 1$ characterizes unitary 1-designs. The frame potential serves as an efficiently computable measure for characterizing the randomness of unitary ensembles and quantifying their closeness to the Haar measure.

While most research focuses on discrete unitary designs, this work investigates continuous unitary design paths. We say an ensemble $\mathcal{E} = \{U(s)\}_{s \in [0,1]}$ is a *path* if it continuously maps $s \in [0, 1]$ to $U(s) \in \mathbb{SU}(d)$. The

path connects two unitaries $U(0)$ and $U(1)$ as its endpoints. When $U(0) = U(1)$, the path is said to be closed (or a loop). The ensemble \mathcal{E} forms a continuous unitary t -design in $\mathbb{SU}(d)$ if, for every polynomial f of degree at most t in the matrix elements of U and U^\dagger ,

$$\int_{[0,1]} f(U(s)) d\mu(s) = \int_{\mathbb{SU}(d)} f(U) dU,$$

where μ is uniform measure on $[0, 1]$ and dU is normalized Haar measure. A natural approach to constructing such paths is to appropriately connect points from an already known discrete unitary design. However, this seems to be quite a non-trivial task. This work is devoted to developing methods to realize this construction principle.

B. Spherical Design

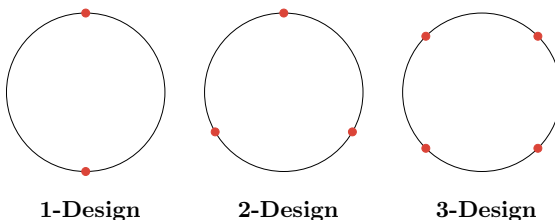
Define $\mathbb{S}^d = \{x \in \mathbb{R}^{d+1} : \|x\| = \sum_{k=1}^{d+1} x_k^2 = 1\}$ to be the d -sphere of the $(d+1)$ -dimensional Euclidean space \mathbb{R}^{d+1} . A spherical design is a configuration of points that are evenly distributed on the sphere. In mathematical definition [55], a finite set of points X on \mathbb{S}^d is a spherical t -design if for every polynomial f in $d+1$ variables of degree t , there is

$$\frac{1}{|X|} \sum_{x \in X} f(x) = \int_{\mathbb{S}^d} f(x) d\mu(x), \quad (5)$$

where μ denotes the standard uniform measure on \mathbb{S}^d , normalized so that $\int_{\mathbb{S}^d} 1 d\mu = 1$.

Some basic facts about spherical designs are given as follows. A spherical t -design is automatically a $(t-1)$ -design. The property of being a t -design is invariant under orthogonal transformations due to the rotational symmetry of μ . Furthermore, the disjoint union of spherical t -designs is itself a t -design. For a set $X \subset \mathbb{S}^d$, it is a 1-design iff $\frac{1}{|X|} \sum_{x \in X} x = 0$, and it is a 2-design iff $\frac{1}{|X|} \sum_{x \in X} x^T x = I_d/d$, where I_d denotes the d -dimensional identity matrix.

Constructing spherical t -designs is generally challenging. There exists a rich field of research on analytic and numerical methods for their construction [81, 82]. The most interesting t -designs are those of minimal cardinality, called tight designs, but are very rare. Tight 1-designs and 2-designs are completely classified. A tight 1-design consists of any pair of antipodal points x and $-x$ on \mathbb{S}^d . A tight 2-design comprises the $d+2$ vertices of a regular simplex inscribed in \mathbb{S}^d . Another basic fact is for \mathbb{S}^1 , a tight t -design is provided by a regular $(t+1)$ -gon:



These tight designs are unique up to orthogonal transformations.

Spherical designs are normally studied in the discrete setting. Recently, Ref. [56] introduced a continuous analogue, defining a spherical t -design curve to be a continuous, piecewise smooth, closed curve $\gamma : [0, 1] \rightarrow \mathbb{S}^d$ with $\gamma(0) = \gamma(1)$, such that for every polynomial f of degree at most t :

$$\frac{1}{\ell(\gamma)} \int_{\gamma} f(\gamma(s)) |\dot{\gamma}(s)| ds = \int_{\mathbb{S}^d} f(x) d\mu(x), \quad (6)$$

where $\dot{\gamma} := d\gamma/ds$ and $\ell(\gamma) := \int_0^1 |\dot{\gamma}(s)| ds$ denotes the arc-length of γ . Several initial approaches to constructing such curves have been explored, such as using graph theory, topological methods, and numerical optimization [56–58]. For example, the following curve

$$\gamma(s) = \frac{1}{\sqrt{d}} (\cos(2\pi s), \sin(2\pi s), \dots, \cos(2\pi ds), \sin(2\pi ds))$$

forms a spherical 2-design curve on \mathbb{S}^{2d-1} . This example will be relevant to our construction of continuous unitary 1-designs later in this work. Despite a handful of explicit examples now being known, as noted in Ref. [57], the general construction of such curves remains challenging, both numerically and analytically.

III. SINGLE-QUBIT

A. Closed Unitary 1-design Path

We begin with the simplest single-qubit system of dimension $d = 2$. Every unitary operator in $\mathbb{SU}(2)$ corresponds to a rotational gate on the Bloch sphere, expressed as $R_{\mathbf{n}}(\theta) = \exp(-i\theta\sigma_{\mathbf{n}}/2)$, where $\theta \in [0, 2\pi]$ is the rotational angle, $\mathbf{n} = (n_x, n_y, n_z)$ is a unit vector in \mathbb{R}^3 specifying the rotational axis, and $\sigma = (\sigma_x, \sigma_y, \sigma_z)$ denotes the vector of Pauli operators. As a first result of this work, we construct a unitary 1-design path in $\mathbb{SU}(2)$ given by

$$U(\theta) = R_{\mathbf{n}_1}(\theta) R_{\mathbf{n}_2}(2\theta), \quad (7)$$

where $\mathbf{n}_1 \perp \mathbf{n}_2$ and $\theta = 2\pi s$ with $s \in [0, 1]$. This forms a closed path based at identity, since $U(0) = U(2\pi) = I$.

We now explain how this path constitutes a unitary 1-design. Let us first consider the specific case with $\mathbf{n}_1 = (0, 0, 1)$ and $\mathbf{n}_2 = (-1, -1, 0)/\sqrt{2}$, so that the unitary path becomes $U(\theta) = e^{-i\theta\sigma_z/2} e^{i2\theta\sigma_{\pi/4}/2}$, where $\sigma_{\pi/4} \equiv (\sigma_x + \sigma_y)/\sqrt{2}$ denotes the operator along the direction $\pi/4$ in the xy -plane. A crucial observation is that this path intersects the single-qubit Pauli group (up to a phase factor) at the points: $U(0) = I$, $U(\pi/2) = iY$, $U(\pi) = iZ$, and $U(3\pi/2) = iX$. Moreover, for any $\varphi \in [0, \pi/2]$, consider the discrete set $\mathbf{U}_{\varphi} = \{U(\varphi + k\pi/2)\}_{k=0}^3$. Clearly, this set can be expressed as the coset $\mathbf{U}_{\varphi} = e^{-i\varphi\sigma_z/2} \mathbf{U}_0 e^{i2\varphi\sigma_{\pi/4}/2}$. Since

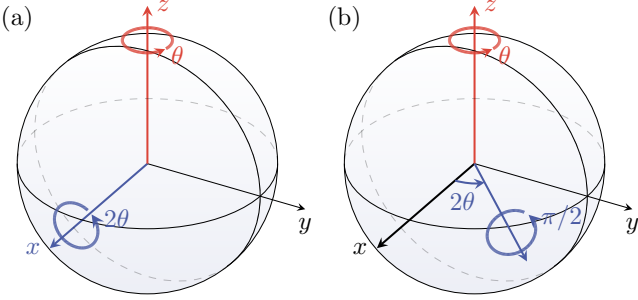


FIG. 1. Two examples of unitary 1-design paths constructed from composition of rotational gates that are controlled by the same angular variable θ . (a) $U(\theta) = R_z(\theta)R_x(2\theta)$: both gates employ fixed rotational axes and varying rotational angles. (b) $U(\theta) = R_z(\theta)R_{2\theta}(\pi/2)$: one gate uses a fixed rotational axis and varying angle, while the other employs a varying rotational axis and fixed angle.

$\mathbf{U}_0 = \{I, i\sigma_y, i\sigma_z, i\sigma_x\}$ is a unitary 1-design and the 1-design property is invariant under either left or right multiplication by a fixed unitary, it follows that \mathbf{U}_φ is also a unitary 1-design for every φ . The union of these 1-designs $\bigcup_{\varphi \in [0, \pi/2)} \mathbf{U}_\varphi$ thus gives our continuous unitary 1-design path.

More generally, the construction remains valid for any pair of mutually perpendicular axes. To see this, consider arbitrary \mathbf{n}_1 and \mathbf{n}_2 satisfying $\mathbf{n}_1 \perp \mathbf{n}_2$. One may first apply a rotation that maps the z -axis to the direction of \mathbf{n}_1 , thereby transforming σ_z into $\sigma_{\mathbf{n}_1}$. Under the same rotation, the original axis corresponding to $\sigma_{\pi/4}$ is mapped to a new axis lying in the plane perpendicular to \mathbf{n}_1 . A subsequent rotation about \mathbf{n}_1 can then align this new axis with \mathbf{n}_2 and meanwhile keeps \mathbf{n}_1 unchanged. The resulting path thus retains the form of Eq. (7) and constitutes a continuous unitary 1-design.

We provide another unitary 1-design path of similar form

$$U(\theta) = R_{\mathbf{n}}(\theta)R_{\mathbf{n}_\perp(2\theta)}(\pi/2), \quad (8)$$

where $\theta \in [0, 2\pi]$, \mathbf{n} is an arbitrary rotational axis, and $\mathbf{n}_\perp(2\theta)$ represents an axis that starts from a vector \mathbf{n}_\perp perpendicular to \mathbf{n} and rotates about \mathbf{n} with angular parameter 2θ . This path is closed and based at the operator $R_{\mathbf{n}_\perp}(\pi/2)$. Unlike the previous construction, here one of the rotational gates has a fixed rotational angle $\pi/2$ but a varying rotational axis, as illustrated in Fig. 1.

B. Continuous Unitary 1-design on $\mathbb{SU}(2)$ and Spherical 2-design curve on \mathbb{S}^3

To explain how unitary 1-design paths are constructed, we first highlight the close relationship between continuous unitary 1-designs and spherical 2-design curves. We begin by identifying the group manifold of $\mathbb{SU}(2)$ with

the 3-sphere \mathbb{S}^3 . Any unitary operator in $\mathbb{SU}(2)$ can be expressed in the form

$$U = \begin{pmatrix} z_1 & z_2 \\ -\bar{z}_2 & \bar{z}_1 \end{pmatrix}, \quad (z_1, z_2) \in \mathbb{C}^2,$$

where $z = (z_1, z_2)$ satisfies the normalization condition $|z_1|^2 + |z_2|^2 = 1$. Furthermore, \mathbb{C}^2 is isomorphic to \mathbb{R}^4 via the mapping $z = (z_1, z_2) = (x_1 + ix_2, x_3 + ix_4) \leftrightarrow x = (x_1, x_2, x_3, x_4)$. The normalization condition then becomes $\|x\| = 1$, which defines the unit 3-sphere \mathbb{S}^3 embedded in \mathbb{R}^4 . This establishes a one-to-one correspondence between $\mathbb{SU}(2)$ and \mathbb{S}^3 , under which the Haar measure on $\mathbb{SU}(2)$ is mapped to the uniform surface measure on \mathbb{S}^3 .

Under the above correspondence, one has that for any traceless Hermitian operator V , the matrix elements of UVU^\dagger are quadratic polynomials in the coordinates x of U , with coefficients depending on V . A spherical 2-design on \mathbb{S}^3 can integrate these quadratic polynomials exactly to match their average over the entire sphere. In this manner, it induces a unitary 1-design in $\mathbb{SU}(2)$. These arguments are presented in more detail in Appendix A. The converse, however, does not hold. A unitary 1-design does not necessarily yield a spherical 2-design, as we will see later.

Therefore, constructing spherical 2-design curves provides a straightforward means to obtain continuous unitary 1-designs. According to Ref. [56], such curves can be generated by continuously connecting the points of a discrete spherical 2-design. The minimal spherical 2-design on \mathbb{S}^3 is given by the five vertices of a regular 4-simplex. Ref. [57] introduced the curve

$$\xi(\theta) = \frac{1}{\sqrt{2}}(\cos \theta, \sin \theta, \cos 2\theta, \sin 2\theta), \quad (9)$$

where $\theta = 2\pi s$ with $s \in [0, 1]$, and showed that it continuously interpolates the minimal 2-design set and is itself a spherical 2-design. The points $\{\xi(2\pi k/5)\}_{k=0}^4$ on ξ correspond to the vertices of the simplex, as verified by checking that their pairwise inner products are all $-1/4$. This construction, however, is not unique. Here, we are interested in another curve with similar behavior,

$$\gamma(\theta) = \frac{1}{\sqrt{2}}(\cos \theta, \sin \theta, \cos 3\theta, -\sin 3\theta), \quad (10)$$

which also connects the same set of vertices as ξ . By direct calculation, the two curves intersect precisely at these vertices

$$\gamma \cap \xi = \{\gamma(2\pi k/5)\}_{k=0}^4 = \{\xi(2\pi k/5)\}_{k=0}^4 = \mathbf{v}(\Delta^4),$$

where we use $\mathbf{v}(\Delta^4)$ to denote the vertex set of the regular 4-simplex Δ^4 ; see Fig. 2(a). The spherical 2-design property of γ and ξ can be confirmed by verifying that both curves satisfy the following sufficient conditions: (i) $\frac{1}{\ell(\gamma)} \int_{\gamma} x_k = 0$ and (ii) $\frac{1}{\ell(\gamma)} \int_{\gamma} x_k x_j = \delta_{kj}/4$.

By using the arc length formula, we obtain $\ell(\xi) = \int_0^1 |\dot{\xi}(s)|ds = \sqrt{10}\pi$ and $\ell(\gamma) = \int_0^1 |\dot{\gamma}(s)|ds = 2\sqrt{5}\pi$. The curve ξ is shorter, suggesting it may be a preferable candidate for a unitary 1-design. However, we observe that γ exhibits redundancy: the point set $\{\gamma(2\pi k/8)\}_{k=0}^7$ maps two-to-one onto the Pauli group 1-design (ignoring global phase), as shown in Fig. 2(b). Examining the expression for γ in Eq. (10), we find that for any $\theta \in [0, \pi]$ there is $\gamma(\theta) = -\gamma(\theta + \pi)$, which implies that the corresponding unitary gates satisfy $U(\theta) = -U(\theta + \pi)$. Although U and $-U$ are distinct elements of $\mathbb{SU}(2)$, they represent the same quantum gate due to the global phase invariance of quantum states. This is a consequence of the fact that $\mathbb{SU}(2)$ is a double cover of the 3-dimensional rotational group $\mathbb{SO}(3)$. To remove this redundancy, we work in the quotient space $\mathbb{SO}(3) \cong \mathbb{SU}(2)/\{I, -I\} \cong \mathbb{S}^3/\{1, -1\}$, identifying antipodal points. The curve γ then descends to a closed curve

$$\tilde{\gamma}(\theta) = \frac{1}{\sqrt{2}}(\cos \frac{\theta}{2}, \sin \frac{\theta}{2}, \cos \frac{3\theta}{2}, -\sin \frac{3\theta}{2}), \quad (11)$$

with length $\ell(\tilde{\gamma}) = \ell(\gamma)/2 = \sqrt{5}\pi$, which is shorter than ξ . Although $\tilde{\gamma}$ is not a spherical 2-design curve in \mathbb{S}^3 , its image in $\mathbb{SU}(2)$, given by

$$U_{\tilde{\gamma}}(\theta) = R_{-z}(\theta)R_{-\pi/2+2\theta}(\pi/2),$$

forms a continuous unitary 1-design, belonging to the class described by Eq. (8).

C. Hopf Fibration

Having presented the explicit design examples, as summarized in Table I, we now delve deeper into the profound geometric intuition and rationale underlying their construction through the lens of the Hopf fibration, basically following the framework established by Refs. [58, 59]. The Hopf map, introduced by Heinz Hopf in a seminal work in 1931 [83], is a projection of the 3-sphere onto the 2-sphere defined by

$$\begin{aligned} \pi : \mathbb{S}^3 &\rightarrow \mathbb{S}^2, \\ (z_1, z_2) &\mapsto (|z_1|^2 - |z_2|^2, \text{Re}(2z_1\bar{z}_2), \text{Im}(2z_1\bar{z}_2)). \end{aligned}$$

This is a continuous surjection with the key property that, the preimage (called *fiber*) of every point on the base sphere \mathbb{S}^2 is a great circle (topologically equivalent to \mathbb{S}^1) in \mathbb{S}^3 . Moreover, fibers over distinct points are mutually disjoint in \mathbb{S}^3 , and their union seamlessly reconstructs the entire \mathbb{S}^3 . This endows \mathbb{S}^3 with a fiber bundle structure, formally denoted as $\mathbb{S}^1 \hookrightarrow \mathbb{S}^3 \rightarrow \mathbb{S}^2$, which effectively partitions \mathbb{S}^3 into a continuous, non-intersecting family of great circles, each uniquely indexed by a point on the 2-sphere:

$$\mathbb{S}^3 = \bigcup_{p \in \mathbb{S}^2} \pi^{-1}(p).$$

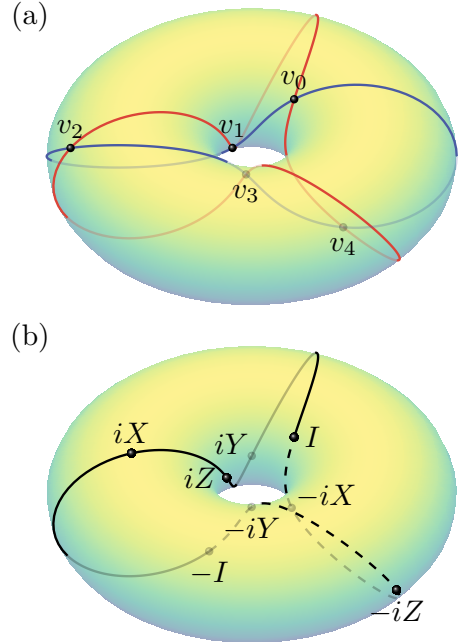


FIG. 2. Visualization of the continuous designs via stereographic projection from $\mathbb{SU}(2) \cong \mathbb{S}^3 \subset \mathbb{R}^4$ to \mathbb{R}^3 . (a) Two continuous spherical 2-design curves γ_ϕ and ξ_ϕ with $\phi = -\pi/4$. They both pass through the same set of points $\{v_0, \dots, v_4\}$ which correspond to the minimal discrete spherical 2-design on \mathbb{S}^3 . They are also unitary 1-design paths. (b) A shorter unitary 1-design path $\tilde{\gamma}_\phi$ is constructed by taking half of γ_ϕ and identifying its endpoints I and $-I$.

The above decomposition naturally motivates a sampling strategy for constructing spherical design curves. One can first sample points from the base space \mathbb{S}^2 , and then sample the corresponding circular fibers attached to these points. To obtain continuous designs, the sampling must be performed in a continuous manner. Ref. [59] presented a concrete realization of this strategy by showing that it is possible to select a $[t/2]$ -design curve from \mathbb{S}^2 and then lift it to a t -design curve on \mathbb{S}^3 . This lifting technique is particularly helpful to understand the geometric feature of the constructed continuous designs.

We now explain how the spherical curve $\gamma(\theta)$ in Eq. (10) is constructed using the lifting technique. We begin by selecting a spherical 1-design curve on \mathbb{S}^2 , typically a meridian great circle parameterized as $(0, \cos \theta, \sin \theta)$. Next, we take its fourfold cover and define the 1-design curve as $\alpha(\theta) = (0, \cos 4\theta, \sin 4\theta)$. We then lift $\alpha(\theta)$ to a curve $\gamma(\theta) = \frac{1}{\sqrt{2}}(e^{i\theta}, e^{-i3\theta})$, which satisfies $\pi(\gamma) = \alpha$. We further clarify that $\gamma(\theta)$ constitutes a spherical 3-design curve on \mathbb{S}^3 . For any point p on the great circle, there exists $\theta_p \in [0, \pi/2]$ such that $\{\alpha(\theta_p + k\pi/2)\}_{k=0}^3$ all coincide with p . The fiber over p , explicitly written as $\pi^{-1}(p) = \left\{ \frac{1}{\sqrt{2}}(e^{i(\theta_p + \varphi)}, e^{-i3\theta_p} e^{i\varphi}) : \varphi \in [0, 2\pi] \right\} \cong \mathbb{S}^1$, is intersected by γ at $\varphi = \{k\pi/2\}$, corresponding to the vertices

Spherical Curves	$\xi = \frac{1}{\sqrt{2}}(e^{i\theta}, e^{i2\theta})$ $\xi' = (\cos \frac{\theta}{2} e^{i3\theta/2}, -\sin \frac{\theta}{2} e^{i3\theta/2})$ $\xi_\phi = (\cos \frac{\theta}{2} e^{i3\theta/2}, -\sin \frac{\theta}{2} e^{i3\theta/2} e^{-i\phi})$	$\gamma = \frac{1}{\sqrt{2}}(e^{i\theta}, e^{-i3\theta})$ $\gamma' = (\cos 2\theta e^{-i\theta}, \sin 2\theta e^{-i\theta})$ $\gamma_\phi = (\cos 2\theta e^{-i\theta}, \sin 2\theta e^{-i\theta} e^{-i\phi})$	$\tilde{\gamma} = \frac{1}{\sqrt{2}}(e^{i\theta/2}, e^{-i3\theta/2})$ $\tilde{\gamma}' = (\cos \theta e^{-i\theta/2}, \sin \theta e^{-i\theta/2})$ $\tilde{\gamma}_\phi = (\cos \theta e^{-i\theta/2}, \sin \theta e^{-i\theta/2} e^{-i\phi})$
Design Property	Spherical 2-design Unitary 1-design	Spherical 3-design Unitary 1-design	Unitary 1-design
Length	$\sqrt{10}\pi$	$2\sqrt{5}\pi$	$\sqrt{5}\pi$

TABLE I. A summary of the spherical curves and their design properties described in Sec. III. The curves are parameterized using $\theta = 2\pi s$, with $s \in [0, 1]$, and a fixed parameter $\phi \in [0, \pi]$.

of a square—a spherical 3-design on the fiber. According to Ref. [59], γ is thus a spherical 3-design on \mathbb{S}^3 . In addition, we note that γ is automatically a spherical 2-design as described in Sec. II.

The curve $\xi(\theta) = (e^{i\theta}, e^{i2\theta})/\sqrt{2}$ in Eq. (9) involves a slightly more analysis. Consider the related curve $\zeta(\theta) = (e^{i\theta}, e^{-i2\theta})/\sqrt{2}$, which clearly exhibits a lifting structure analogous to $\xi(\theta)$: (i) its projection $\pi(\zeta)$ covers a great circle of \mathbb{S}^2 , and (ii) its intersection with any fiber over that great circle corresponds to a regular triangle—a 2-design on the fiber \mathbb{S}^1 . Hence, ζ forms a spherical

2-design on \mathbb{S}^3 . Since ξ can be obtained from ζ via the transformation $\xi = T(\zeta)$, where $T = \text{diag}(1, 1, 1, -1)$ represents an inversion, it follows that ξ is also a 2-design curve.

D. Closed Unitary 1-design Path Based at Identity

We are in particular interested in constructing unitary 1-design paths based at the identity, as many applications, such as quantum control, require the evolution to start from the identity operation. This can be readily achieved in several ways.

First, if $\{U(\theta) : \theta \in [0, 2\pi]\}$ is a unitary 1-design loop with $U(0) \neq I$, then applying $U^\dagger(0)$ to the entire set yields $\{U(\theta)U^\dagger(0) : \theta \in [0, 2\pi]\}$, which remains a unitary 1-design loop but now is based at identity I .

Second, we may exploit the rotational invariance of the spherical design property: any known spherical 2-design curve gives rise to a family of equivalent curves under rotations. By applying a suitable rotation, we align the curves to start at $(1, 0, 0, 0) \in \mathbb{S}^3$, corresponding to the identity gate. Explicitly, using the rotation matrix

$$R = \frac{1}{\sqrt{2}} \begin{pmatrix} 1 & 0 & 1 & 0 \\ 0 & 1 & 0 & 1 \\ 0 & 1 & 0 & -1 \\ -1 & 0 & 1 & 0 \end{pmatrix}, \quad \det(R) = 1,$$

we obtain the following curves

$$\xi' \equiv R(\xi) = (\cos \frac{\theta}{2} e^{i3\theta/2}, -\sin \frac{\theta}{2} e^{i3\theta/2}), \quad (12)$$

$$\gamma' \equiv R(\gamma) = (\cos 2\theta e^{-i\theta}, \sin 2\theta e^{-i\theta}), \quad (13)$$

$$\tilde{\gamma}' \equiv R(\tilde{\gamma}) = (\cos \theta e^{-i\theta/2}, \sin \theta e^{-i\theta/2}), \quad (14)$$

where $\theta = 2\pi s$ with $s \in [0, 1]$.

Third, we may alternatively employ the lifting technique from the outset to obtain similar results. For the curve corresponding to Eq. (12), we begin by selecting a spherical 1-design curve on \mathbb{S}^2 starting at the base point $(1, 0, 0)$. Specifically, we take the great circle $(\cos \theta, \sin \theta, 0)$ and use its threefold cover, defining the resulting 1-design curve as $\alpha(\theta) = (\cos 3\theta, \sin 3\theta, 0)$.

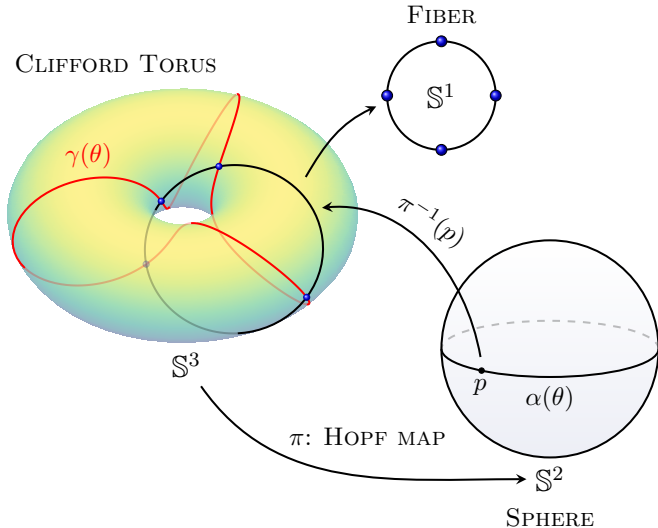


FIG. 3. Illustration of the construction and geometrical properties of the spherical 3-design curve γ . Hopf fibration represents the group $\mathbb{SU}(2) \cong \mathbb{S}^3$ as a family of circles (fibers) indexed by the base space \mathbb{S}^2 . The construction begins by selecting a spherical 1-design α (a great circle) on the base sphere. The preimage of any point p on α under the Hopf map is a fiber (circle), and the preimage of the entire great circle α forms a Clifford torus in \mathbb{S}^3 . The curve γ is constructed as a lift of α such that it intersects each fiber at exactly four symmetric points—forming a spherical 3-design on that fiber. In this way, γ itself constitutes a continuous spherical 3-design curve.

Subsequently, we lift it to the following curve $\varsigma(\theta) = (\cos(3\theta/2)e^{-i\theta/2}, \sin(3\theta/2)e^{-i\theta/2})$ that starts at $\varsigma(0) = (1, 0, 0, 0)$. It is straightforward to verify that this curve satisfies $\pi(\varsigma) = \alpha$, and that its intersection with each fiber of the great circle forms a 2-design on that fiber. Consequently, $\varsigma(\theta)$ constitutes a spherical 2-design curve. Finally, we obtain the following curve ξ_ϕ as

$$\xi_\phi(\theta) = \left(\cos \frac{\theta}{2} e^{i3\theta/2}, -\sin \frac{\theta}{2} e^{i3\theta/2} e^{-i\phi} \right) \quad (15)$$

from the transformation $\xi_\phi = Q(\varsigma)$ with

$$Q(\phi) = \begin{pmatrix} 1 & 0 & 0 & 0 \\ 0 & 0 & 1 & 0 \\ 0 & \cos \phi & 0 & -\sin \phi \\ 0 & \sin \phi & 0 & \cos \phi \end{pmatrix}, \quad \det(Q) = 1.$$

According to the analysis in Sec. II, the set $\{\xi_\phi(\theta)\}_{\phi \in [0, \pi]}$ also constitutes a family of spherical 2-design curves.

For the curves related to Eqs. (13) and (14), we consider a great circle on \mathbb{S}^2 obtained by rotating the equator about the $(1, 0, 0)$ -axis by an angle $\phi \in [0, \pi]$, i.e., $(\cos \theta, \sin \theta \cos \phi, \sin \theta \sin \phi)$. We see that ϕ plays the role of a relative phase here. We then take its fourfold cover $\alpha_\phi(\theta) = (\cos 4\theta, \sin 4\theta \cos \phi, \sin 4\theta \sin \phi)$ as a spherical 1-design curve, which is then lifted to the following curve

$$\gamma_\phi(\theta) = (\cos 2\theta e^{-i\theta}, \sin 2\theta e^{-i\theta} e^{-i\phi}). \quad (16)$$

It satisfies $\pi(\gamma_\phi) = \alpha_\phi$, with intersections on each fiber forming a 3-design on that fiber. Thus, $\{\gamma_\phi(\theta)\}_{\phi \in [0, \pi]}$ constitutes a family of spherical 3-design curves. Taking half of these curves, we get

$$\tilde{\gamma}_\phi(\theta) = (\cos \theta e^{-i\theta/2}, \sin \theta e^{-i\theta/2} e^{-i\phi}), \quad (17)$$

which corresponds to a family of unitary 1-design loops $U_\phi(\theta) = R_z(\theta)R_\phi(2\theta)$. We can use Hopf map and stereographic projection to visualize the construction process, as shown in Fig. 3, more details are given in Appendix B.

E. Open Unitary 1-design Path

So far, we have considered only closed unitary 1-design paths. We now present a method for constructing an open unitary 1-design path from a closed one. Without loss of generality, we take the identity I as the starting point and an arbitrary target operator U^* as the ending point.

Consider, for example, the closed unitary 1-design path $\gamma : s \in [0, 1] \mapsto U(\theta = 2\pi s) = e^{-i\theta\sigma_z/2} e^{i2\theta\sigma_{\pi/4}/2}$. If U^* does not lie on γ , there exists an equivalent unitary 1-design path $WU(\theta)W^\dagger$ that passes through U^* . To show this, we introduce a metric f on $\mathbb{SU}(2)$ defined by $f(U, V) = |\text{Tr}(UV^\dagger)|/2$, which takes values in $[0, 1]$. The distance from any point on γ to the identity is given by $f(U(\theta), I) = |\cos 2\theta \cos(\theta/4)|$, and this expression covers

the entire interval $[0, 1]$. Therefore, for any U^* , there exists some θ^* such that $f(U^*, I) = f(U(\theta^*), I)$. Moreover, since $\text{Tr } U = \text{Tr } V$ and $\det U = \det V$ imply the existence of a unitary W such that $U = WVW^\dagger$, we may conjugate γ by a suitable W to obtain a closed unitary 1-design path containing U^* .

Based on the above analysis, suppose that there exists $s^* \in [0, 1]$ such that $U(\theta^* = 2\pi s^*) = U^*$. We then define a path $\alpha(s) = \gamma((1 + s^*)s)$ for $s \in [0, 1]$, which starts from I and ends at U^* . An illustration is provided in Fig. 4(a). Since $\gamma(s)$ is a closed path, the segment $\gamma([0, s^*])$ is traversed twice by α , whereas $\gamma([s^*, 1])$ is traversed only once, resulting in nonuniform sampling along γ . To achieve a more uniform coverage, we reparameterize the path to obtain a new one, $\beta(s)$, which can be directly expressed in terms of γ as $\beta(s) = \alpha(\varphi(s)) = \gamma((1 + s^*)\varphi(s))$, where $\varphi : [0, 1] \rightarrow [0, 1]$ is a piecewise linear reparameterization that adjusts the relative lengths of the three subintervals $[0, s^*/2]$, $[s^*/2, 1 - s^*/2]$, and $[1 - s^*/2, 1]$ so that they occupy the proportions $s^*/(1 + s^*)$, $1/(1 + s^*) - s^*/(1 + s^*)$, and $1 - 1/(1 + s^*)$ of the full parameter range for α . This construction redistributes the sampling density along γ while preserving the endpoints. The resulting path β is homotopic to α and shares the same endpoints:

$$\beta(s) = \begin{cases} \alpha \left(\frac{2s}{1 + s^*} \right), & s \in [0, s^*/2], \\ \alpha \left(\frac{s + s^*/2}{1 + s^*} \right), & s \in [s^*/2, 1 - s^*/2], \\ \alpha \left(\frac{2s - 1 + s^*}{1 + s^*} \right), & s \in [1 - s^*/2, 1]. \end{cases}$$

It should be noticed that, unlike our previous constructions, for this path β , a uniform sampling $\{\beta(k/N)\}_{k=1}^N$ actually yields an approximate unitary 1-design for finite N , and its distance to an exact unitary 1-design vanishes as N goes large.

As a concrete example, Fig. 4(b) shows the explicit form of the open unitary 1-design path for the target $U^* = Z$, constructed according to the above formula. We sample this path at equiangular points to obtain a discrete ensemble of unitaries $\mathcal{E}_N = \{U_k = \beta(k/N)\}_{k=1}^N$ and compute the corresponding frame potential $\mathcal{F}_{\mathcal{E}_N}^{(1)} = |\text{Tr}(U_k U_j)|^2/N^2$. It is found that $\mathcal{F}_{\mathcal{E}_N}^{(1)}$ converges exponentially fast in N to the Haar value $\mathcal{F}_{\text{Haar}}^{(1)} = 1$, reflecting the unitary 1-design property.

IV. HIGHER-DIMENSIONAL SYSTEMS

We have presented various constructions of continuous unitary designs for the qubit system. In this section, we extend these conceptual frameworks and analytical methods to higher-dimensional systems, introducing several approaches for constructing unitary 1-design paths within the $\mathbb{SU}(d)$ group.

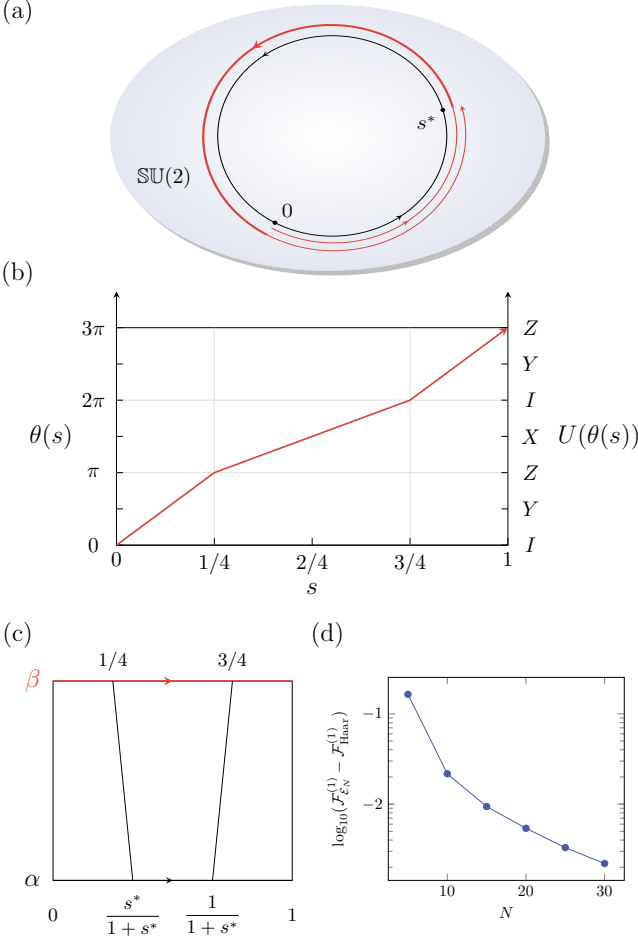


FIG. 4. (a) Illustration of constructing an open unitary 1-design path from a closed one. (b) An open unitary 1-design path connecting I to Z (global phase ignored, and $s^* = 1/2$), derived from $U(\theta) = e^{-i\theta\sigma_z/2} e^{i2\theta\sigma_{\pi/4}/2}$ with θ a piecewise linear function of s . (c) From the closed path γ , we first extract an open path α connecting I to Z , and then generate a homotopic, unitary 1-design path β . (d) Finite sampling of β yields an approximate unitary 1-design, which rapidly converges to an exact unitary 1-design as the number of sampling points increases.

A. Multi-qubit System

Generalizing the qubit unitary 1-design path to multi-qubit systems is straightforward.

For two-qubit system, we present a unitary 1-design path as the following

$$U(\theta) = (e^{-i\theta\sigma_z/2} e^{i2\theta\sigma_{\pi/4}/2}) \otimes (e^{-i4\theta\sigma_z/2} e^{i8\theta\sigma_{\pi/4}/2}). \quad (18)$$

To verify this construction, we first establish a general result: Let $\{U_b\}_{b \in \mathbb{Z}_B}$ be a B -element unitary 1-design in $\mathbb{SU}(2)$, and for each b let there be an associated A -element unitary 1-design ensemble $\{U_a^{(b)}\}_{a \in \mathbb{Z}_A}$ in $\mathbb{SU}(2)$ (which need not be identical for different b). Then the AB -element ensemble $\{U_a^{(b)} \otimes U_b\}$ forms a unitary 1-design

in $\mathbb{SU}(4)$. This can be demonstrated by examining its action on Pauli operators:

$$\begin{aligned} & \frac{1}{AB} \sum_{a,b} \left(U_a^{(b)} \otimes U_b \right) P_\mu \otimes P_\nu \left(U_a^{(b)} \otimes U_b \right)^\dagger \\ &= \frac{1}{B} \sum_b \frac{1}{A} \left[\sum_a U_a^{(b)} P_\mu (U_a^{(b)})^\dagger \right] \otimes U_b P_\nu U_b^\dagger \\ &= \frac{1}{B} \sum_b \frac{\text{Tr } P_\mu}{2} I \otimes (U_b P_\nu U_b^\dagger) \\ &= \frac{\text{Tr } P_\mu \text{Tr } P_\nu}{4} I \\ &= \frac{\text{Tr}(P_\mu \otimes P_\nu)}{4} I. \end{aligned}$$

Now we use this result to show that Eq. (18) defines a 1-design path. Consider the path at the discrete set $\{U(\theta_k)\}$ where $\theta_k = 2\pi k/16$ for $k \in \mathbb{Z}_{16}$. Decomposing $k = 4a + b$ with $a, b \in \mathbb{Z}_4$, and denoting $R_1 = e^{-i\theta_1\sigma_z/2}$ and $R_2 = e^{i2\theta_1\sigma_{\pi/4}/2}$ with $\theta_1 = 2\pi/16$, we obtain

$$U(\theta_k) = U\left(\frac{2\pi(4a+b)}{16}\right) = (R_1^b P_a R_2^b) \otimes P_b,$$

in which $P_0 = I$, $P_1 = iY$, $P_2 = iZ$, $P_3 = iX$. Clearly, $\{P_b\}_{b \in \mathbb{Z}_3}$ is a unitary 1-design, and for each b , $\{R_1^b P_a R_2^b\}_{a \in \mathbb{Z}_3}$ is a 1-design, hence the set $\{U(\theta_k)\}$ constitutes a 1-design. Next, for any $\varphi \in [0, \pi/16]$, the discrete set $\{U(\theta_k + \varphi)\}$ is simply the set $\{U(\theta_k)\}$ left-multiplied by $e^{-i\varphi\sigma_z/2} \otimes e^{-i4\varphi\sigma_z/2}$ and right-multiplied by $e^{i2\varphi\sigma_{\pi/4}/2} \otimes e^{i8\varphi\sigma_{\pi/4}/2}$, and thus also forms a 1-design. Therefore, we conclude that the entire path defined in Eq. (18) constitutes a unitary 1-design path.

This construction generalizes naturally to an N -qubit system as

$$U(\theta) = \bigotimes_{m=1}^N (R_{\mathbf{n}_{m1}} (4^{N-1}\theta) R_{\mathbf{n}_{m2}} (2 \times 4^{N-1}\theta)) \quad (19)$$

where the rotational axes satisfy $\mathbf{n}_{m1} \perp \mathbf{n}_{m2}$ for all $m = 1, \dots, N$.

B. Construction Based on Fiber Bundle Theory

We have seen that for qubit system, unitary 1-designs can be directly derived from spherical designs due to the isomorphism $\mathbb{SU}(2) \cong \mathbb{S}^3$. For general qudit systems, the situation is more subtle since $\mathbb{SU}(d)$ is not isomorphic to a sphere of dimension $2d-1$. Nevertheless, we can leverage the fiber bundle structure of $\mathbb{SU}(d)$, and spherical designs remain instrumental in constructing unitary designs. In what follows, we first demonstrate this approach for $d = 3$ dimensional systems, then proceed to the general case.

Consider the qutrit system. We analyze the topological and manifold structure of $\mathbb{SU}(3)$, basically following [84]. $\mathbb{SU}(3)$ is a simply connected, compact, 8-dimensional

manifold that is not diffeomorphic to \mathbb{S}^8 . Indeed, it admits the well-known fibration

$$\mathbb{SU}(2) \hookrightarrow \mathbb{SU}(3) \xrightarrow{\pi} \mathbb{S}^5, \quad (20)$$

where $\mathbb{SU}(3)$ is the total space, \mathbb{S}^5 is the base space and $\mathbb{SU}(2) \cong \mathbb{S}^3$ is the fiber. According to the theory of bundles, $\mathbb{SU}(3)$ is the unique (up to isomorphism) nontrivial $\mathbb{SU}(2)$ -bundle over \mathbb{S}^5 .

We now explain the structure in detail. Let ι denote the inclusion of $\mathbb{SU}(2)$ into $\mathbb{SU}(3)$

$$\iota : \mathbb{SU}(2) \rightarrow \mathbb{SU}(3), \quad \begin{pmatrix} z_1 & z_2 \\ -\bar{z}_2 & \bar{z}_1 \end{pmatrix} \mapsto \begin{pmatrix} 1 & 0 & 0 \\ 0 & z_1 & z_2 \\ 0 & -\bar{z}_2 & \bar{z}_1 \end{pmatrix}.$$

Clearly $\iota(\mathbb{SU}(2)) \cong \mathbb{SU}(2)$ forms a subgroup of $\mathbb{SU}(3)$. Consider the left action of $\iota(\mathbb{SU}(2))$ on $\mathbb{SU}(3)$, defined by $(W, U) \mapsto WU$ for $W \in \iota(\mathbb{SU}(2))$ and $U \in \mathbb{SU}(3)$. This left action preserves the first row of U . Conversely, if two matrices U_1 and U_2 share the same first row, then there exists $W \in \iota(\mathbb{SU}(2))$ such that $WU_1 = WU_2$. Thus, for each U in $\mathbb{SU}(3)$, its right coset $\{WU : W \in \iota(\mathbb{SU}(2))\}$ consists of all matrices with the same first row, and each distinct first row corresponds uniquely to a single right coset. This partitions the entire set $\mathbb{SU}(3)$ into cosets. We define the projection π mapping each unitary matrix to its first row:

$$\begin{aligned} \pi : \mathbb{SU}(3) &\rightarrow \mathbb{S}^5, \\ U = \begin{pmatrix} c_1 & c_2 & c_3 \\ * & * & * \\ * & * & * \end{pmatrix} &\mapsto c = (c_1 \ c_2 \ c_3), \end{aligned}$$

where the row vector c satisfies $|c_1|^2 + |c_2|^2 + |c_3|^2 = 1$, so $c \in \mathbb{S}^5$. By the preceding analysis, each point in \mathbb{S}^5 corresponds to a unique $\mathbb{SU}(2)$ right coset in $\mathbb{SU}(3)$. That is, for each $c \in \mathbb{S}^5$, the preimage $\pi^{-1}(c) \cong \mathbb{SU}(2)$. Hence, \mathbb{S}^5 serves as the base space and $\mathbb{SU}(2)$ as the fiber.

The next step is *local trivialization*. The fact that $\mathbb{SU}(3)$ is a nontrivial $\mathbb{SU}(2)$ -bundle over \mathbb{S}^5 means that $\mathbb{SU}(3)$ looks, locally, like a product $\mathbb{S}^3 \times \mathbb{S}^5$ since $\mathbb{SU}(2) \cong \mathbb{S}^3$, but not globally. The \mathbb{S}^3 fiber is twisted over the \mathbb{S}^5 base in a non-trivial manner. To enable local coordinateization, we consider an open subset of $\mathbb{SU}(3)$

$$\mathcal{M} = \{U \in \mathbb{SU}(3) : |c_3| > 0\},$$

whose projection is an open subset of \mathbb{S}^5

$$M = \pi(\mathcal{M}) = \{c \in \mathbb{S}^5 : |c_3| > 0\}.$$

For each point $c \in M \subset \mathbb{S}^5$, we can select a coset representative by completing the other two rows via the Gram-Schmidt process

$$(c_1 \ c_2 \ c_3) \mapsto \begin{pmatrix} c_1 & c_2 & c_3 \\ 0 & \bar{c}_3 & -\bar{c}_2 \\ \sqrt{1-|c_1|^2} & \frac{-c_2\bar{c}_1}{\sqrt{1-|c_1|^2}} & \frac{-c_3\bar{c}_1}{\sqrt{1-|c_1|^2}} \end{pmatrix}.$$

Since $|c_3| > 0$, the denominator $\sqrt{1-|c_1|^2}$ does not vanish, ensuring the matrix is well-defined. This provides a representative element in the coset fiber $\pi^{-1}(c) \subset \mathcal{M}$, and the full coset can be obtained by left action of $\iota(\mathbb{SU}(2))$ over this element. Thus, any $U \in \mathcal{M}$ is parameterized as:

$$\begin{pmatrix} 1 & 0 & 0 \\ 0 & z_1 & z_2 \\ 0 & -\bar{z}_2 & \bar{z}_1 \end{pmatrix} \begin{pmatrix} c_1 & c_2 & c_3 \\ 0 & \bar{c}_3 & -\bar{c}_2 \\ \sqrt{1-|c_1|^2} & \frac{-c_2\bar{c}_1}{\sqrt{1-|c_1|^2}} & \frac{-c_3\bar{c}_1}{\sqrt{1-|c_1|^2}} \end{pmatrix}.$$

The consequence is that, each unitary in $\mathcal{M} \subset \mathbb{SU}(3)$ is then described by eight local coordinates: a complex two-component unit vector $|z_1|^2 + |z_2|^2 = 1$ and a complex three-component unit vector $|c_1|^2 + |c_2|^2 + |c_3|^2 = 1$ with $|c_3| > 0$.

We note that the complement set $\mathcal{M}^c = \{U \in \mathbb{SU}(3) : c_3 = 0\}$ forms a six-dimensional subset of $\mathbb{SU}(3)$ with vanishing measure. Therefore, \mathcal{M} covers almost full of $\mathbb{SU}(3)$. In this sense, a design set on \mathcal{M} should effectively be a design set on $\mathbb{SU}(3)$.

To construct a 1-design path in $\mathbb{SU}(3)$, we select a 2-design curve in the base space \mathbb{S}^5 and a 2-design point set in \mathbb{S}^3 , then combine them appropriately. Recall that for \mathbb{S}^3 , we have studied the spherical 2-design curve $\xi(\theta) = \frac{1}{\sqrt{2}}(e^{i\theta}, e^{i2\theta})$. A key property of this curve is that the discrete set $\{\xi(2\pi k/5 + \varphi)\}_{k=0}^4$ forms a 2-design point set for any $\varphi \in [0, 2\pi/5]$. This motivates us to seek a 2-design curve in \mathbb{S}^5 with a periodicity of $5(2\pi)$. We choose the canonical 2-design curve

$$\alpha(\theta) = \frac{1}{\sqrt{3}}(1, e^{i\theta}, e^{i2\theta}),$$

and lift it to a curve $\gamma(\theta)$ in the fiber bundle \mathcal{M}

$$\gamma(\theta) = \left\{ \frac{1}{\sqrt{2}}(e^{i\theta}, e^{i2\theta}), \quad \frac{1}{\sqrt{3}}(1, e^{i5\theta}, e^{i10\theta}) \right\}, \quad (21)$$

where $\theta = 2\pi s$ ($s \in [0, 1]$). As before, this curve satisfies two essential properties: (i) its projection runs through α exactly 5 times, satisfying $(\pi \circ \gamma)(s) = \alpha(5s - \lfloor 5s \rfloor)$, and (ii) γ intersects each fiber exactly five times, with the intersection points forming a 2-design set of the fiber. Specifically, for every s , we have $\gamma([0, 1]) \cap \pi^{-1}(\alpha(s)) = \{\gamma(k/5 + s) : k = 0, \dots, 4\}$. At last, our constructed unitary 1-design path takes the form

$$U(\theta) = \begin{pmatrix} 1 & 0 & 0 \\ 0 & z & z^2 \\ 0 & -\bar{z}^2 & \bar{z} \end{pmatrix} \begin{pmatrix} \frac{1}{\sqrt{3}} & \frac{z^5}{\sqrt{3}} & \frac{z^{10}}{\sqrt{3}} \\ 0 & \frac{\bar{z}^{10}}{\sqrt{2}} & -\frac{\bar{z}^5}{\sqrt{2}} \\ \frac{\sqrt{2}}{\sqrt{3}} & -\frac{z^5}{\sqrt{6}} & -\frac{z^{10}}{\sqrt{6}} \end{pmatrix}, \quad (22)$$

where $z = e^{i\theta}$. The design property can be verified by computing the frame potential. It is found that the path

sampled at the N discrete points $\{\theta = 2\pi k/N + \varphi\}_{k=0}^{N-1}$ forms a unitary 1-design for any $\varphi \in [0, 2\pi/N)$ when $N \geq 25$.

In general, the special unitary group $\mathbb{SU}(d)$ possesses a natural principal fiber bundle structure, topologically characterized by an iterative sequence of sphere fibrations. Specifically, $\mathbb{SU}(d)$ forms a locally trivial fiber bundle over the base \mathbb{S}^{2d-1} with fiber $\mathbb{SU}(d-1)$, a structure arising from the transitive action of $\mathbb{SU}(d)$ on the unit sphere in \mathbb{C}^d . This fibration,

$$\mathbb{SU}(d-1) \hookrightarrow \mathbb{SU}(d) \rightarrow \mathbb{S}^{2d-1}$$

where π maps a unitary matrix to its first row, induces an inductive decomposition. Iterating this construction reveals $\mathbb{SU}(d)$ as a twisted product of the odd-dimensional spheres $\mathbb{S}^{2d-1}, \mathbb{S}^{2d-3}, \dots, \mathbb{S}^3$, fully characterizing its underlying manifold.

Leveraging this structure, we construct unitary design paths inductively. Assume we have α as a unitary design path in $\mathbb{SU}(d-1)$ such that its discrete sampling at N_{d-1} points $\{\theta = 2\pi k/N_{d-1} + \varphi\}_{k=0}^{N_{d-1}-1}$ forms a 1-design for any $\varphi \in [0, 2\pi/N_{d-1})$ when $N \geq N_{d-1}$. The construction proceeds in two steps: (i) choose the spherical 2-design curve in \mathbb{S}^{2d-1} given by $(1, e^{i\theta}, \dots, e^{i(d-1)\theta})/\sqrt{d}$; (ii) lift it to the curve $\{\alpha(\theta), (1, e^{iN_{d-1}\theta}, \dots, e^{i(d-1)N_{d-1}\theta})/\sqrt{d}\}$. As an example, the unitary 1-design path for $d = 3$ in Eq. (21) has $N_3 = 25$, so a unitary 1-design path for $d = 4$ can take the form

$$\gamma(\theta) = \left\{ \frac{1}{\sqrt{2}} \begin{pmatrix} e^{i\theta} \\ e^{i2\theta} \end{pmatrix}, \frac{1}{\sqrt{3}} \begin{pmatrix} 1 \\ e^{i5\theta} \\ e^{i10\theta} \end{pmatrix}, \frac{1}{\sqrt{4}} \begin{pmatrix} 1 \\ e^{i25\theta} \\ e^{i50\theta} \\ e^{i75\theta} \end{pmatrix} \right\}.$$

C. Construction Based on Heisenberg-Weyl Group

Our alternative approach is grounded in the well-established framework of the Heisenberg-Weyl (HW) group [85]. For a qudit of dimension $d \geq 2$, we define the shift operator X and the phase operator Z in the natural basis $\{|j\rangle : j = 0, \dots, d-1\}$ as

$$X = \sum_{j=0}^{d-1} |j+1 \pmod{d}\rangle\langle j|, \quad Z = \sum_{j=0}^{d-1} \omega^j |j\rangle\langle j|,$$

where $\omega = e^{i2\pi/d}$ is the primitive d -th root of unity satisfying $\omega^d = 1$. These operators are unitary and obey $X^d = I$ and $Z^d = I$. The HW group is generated by X and Z as the set of d^2 unitary operators $\{\Lambda_{ab} = X^a Z^b\}$ with $a, b \in \mathbb{Z}_d = \{0, \dots, d-1\}$. All non-identity elements of this group are traceless.

The HW group generalizes the Pauli group to higher dimensions and forms a unitary 1-design. It has been used, for example, in constructing universal dynamical

decoupling sequences [86]. Leveraging this group structure, we define a continuous, closed unitary path as follows:

$$U(\theta) = W \left[\sum_{k=0}^{d-1} e^{ik\theta} |k\rangle\langle k| \right] W^\dagger \left[\sum_{k=0}^{d-1} e^{ikd\theta} |k\rangle\langle k| \right], \quad (23)$$

where W is the generalized Walsh-Hadamard transform

$$W = \frac{1}{\sqrt{d}} \sum_{k,j=0}^{d-1} \omega^{-kj} |k\rangle\langle j|,$$

which interchanges the shift and phase operators via the conjugation relation $WZ^a W^\dagger = X^a$ for all $a \in \mathbb{Z}_d$. The qutrit W gate has been experimentally implemented in, e.g., superconducting system [87]. One may readily verify that $U(0) = U(2\pi) = 0$, confirming that the path is closed.

To demonstrate that the path Eq. (23) yields a unitary 1-design, we first examine its values at the discrete set of equiangular points $\theta_k = 2\pi k/d^2$ for $k \in \mathbb{Z}_{d^2}$. Decomposing the index k as $k = a \cdot d + b$ with $a, b \in \mathbb{Z}_d$, we write $\theta_k = 2\pi a/d + 2\pi b/d^2$. At these points, the unitary becomes:

$$U(\theta_k) = Q^b X^a Z^b,$$

where

$$Q = W \begin{pmatrix} 1 & 0 & \dots & 0 \\ 0 & e^{i2\pi/d^2} & \dots & 0 \\ \vdots & \vdots & \ddots & \vdots \\ 0 & 0 & \dots & e^{i2\pi(d-1)/d^2} \end{pmatrix} W^\dagger.$$

Thus, the set $U(\theta_k)_{k=0}^{d^2-1}$ corresponds to HW group elements multiplied on the left by powers of Q . We now show that the presence of Q does not affect the 1-design property.

The proof relies on two key properties of the HW group. First, from the basic commutation relation $\omega XZ = ZX$, one derives the general relation $X^\mu Z^\nu = \omega^{-\mu\nu} Z^\nu X^\mu$, which implies the conjugation rule $\Lambda_{ab} \Lambda_{\mu\nu} \Lambda_{ab}^\dagger = \omega^{-a\nu+b\mu} \Lambda_{\mu\nu}$. Second, the HW group forms an orthogonal operator basis. Hence, if the set $\{U(\theta_k)\}_{k=0}^{d^2-1}$ averages every HW operator except the identity to zero, then it can average out all traceless Hermitian operators, thus will be a unitary 1-design.

We now verify this condition for an arbitrary non-identity HW operator $\Lambda_{\mu\nu}$ (i.e., $(\mu, \nu) \neq (0, 0)$). Consider the average

$$\begin{aligned} \sum_{k=0}^{d^2-1} U(\theta_k) \Lambda_{\mu\nu} U(\theta_k)^\dagger &= \sum_{a,b=0}^{d-1} Q^b \Lambda_{ab} \Lambda_{\mu\nu} \Lambda_{ab}^\dagger Q^{b\dagger} \\ &= \sum_{a,b=0}^{d-1} \omega^{-a\nu+b\mu} Q^b \Lambda_{\mu\nu} Q^{b\dagger}. \end{aligned}$$

We analyze two possible cases. First, if $\mu \neq 0$ and $\nu = 0$, then $\Lambda_{\mu\nu} = X^\mu$, and since Q commutes with X , we have

$$\sum_{a,b=0}^{d-1} \omega^{-a\nu+b\mu} Q^b X^\mu Q^{b\dagger} = \sum_a^{d-1} \omega^{-a\nu} X^\mu \left[\sum_{b=0}^{d-1} \omega^{b\mu} \right] = 0.$$

Second, if $\nu \neq 0$, then

$$\sum_{b=0}^{d-1} \omega^{b\mu} Q^b \Lambda_{\mu\nu} Q^{b\dagger} \left[\sum_{a=0}^{d-1} \omega^{-a\nu} \right] = 0,$$

From the derivation we see that, since Q is commutative with X and the summations ensure cancellation, the presence of Q does not alter the result. This confirms that the set $U(\theta_k)$ is a unitary 1-design.

We denote $\mathbf{U}_0 = \{U(\theta_k)\}_{k=0}^{d^2-1}$, and define for any $\varphi \in [0, 2\pi/d^2)$ the shifted set $\mathbf{U}_\varphi = U(\theta_k + \varphi)k = 0^{d^2-1}$. These sets are related by:

$$\mathbf{U}_\varphi = \left[W \sum_{k=0}^{d-1} e^{ik\varphi} |k\rangle\langle k| W^\dagger \right] \mathbf{U}_0 \left[\sum_{k=0}^{d-1} e^{ikd\varphi} |k\rangle\langle k| \right].$$

Since \mathbf{U}_0 is a unitary 1-design, and the above relation represents a unitary conjugation and multiplication (which preserve the 1-design property), it follows that \mathbf{U}_φ is also a unitary 1-design. Consequently, the union $\bigcup_{\varphi \in [0, 2\pi/d^2)} \mathbf{U}_\varphi$, which comprises the entire path, forms a unitary 1-design.

V. APPLICATION: UNIVERSALLY ROBUST CONTROL

Continuous unitary designs have natural applications in the field of robust quantum control. In the following, we demonstrate that our constructed continuous unitary 1-design paths provide analytical solutions for achieving universally robust control (URC).

A. Theory

We consider a quantum system with a Hamiltonian H_S exposed to a noisy environment. The noise is modeled by a perturbation V , characterized by unknown amplitudes along arbitrary directions in the Liouvillian space. Our objective is to design a time-varying control pulse $u(t)$ of duration $0 \leq t \leq T$ that generates a control Hamiltonian $H_C(u(t))$ to realize a predefined target gate \bar{U} while optimally suppressing the noise effects of V . Without loss of generality, we omit the identity component from H_C and V as it only induces a global phase, rendering both operators traceless.

The system's total evolution is described by

$$U_{\text{tot}}(t) = \mathcal{T} \exp \left\{ -i \int_0^t [H_S + H_C(t_1) + V] dt_1 \right\},$$

where \mathcal{T} denotes the time-ordering operator. We assume the system is fully controllable, meaning control solutions exist to realize any target gate in the absence of noise. However, noise causes the actual evolution to deviate from the ideal target, introducing errors. This deviation can be quantified by the gate fidelity

$$F(\bar{U}, U_{\text{tot}}) = \frac{|\text{Tr}[\bar{U}^\dagger U_{\text{tot}}(T)]|^2}{d^2}, \quad (24)$$

where d is the system dimension. To proceed analytically, we assume that the noise term V is small relative to H_S , allowing us to employ the Dyson perturbative series [88]. In this framework, the total evolution operator is expanded as $U_{\text{tot}}(T) = U(T)[I + D^{(1)} + D^{(2)} + \dots]$, where $U(T)$ is the noise-free evolution operator that implements the target gate, and

$$D^{(k)} = (-i)^k \int_{0 < t_k < \dots < t_1 < T} \prod_{j=1}^k U^\dagger(t_j) V U(t_j) dt_j$$

represents the k th-order error term due to presence of V . Truncating the expansion at second order yields an approximate fidelity of

$$F \approx 1 - \frac{1}{d} \text{Tr} \left[\left(\int_0^T U^\dagger(t) V U(t) dt \right)^2 \right]. \quad (25)$$

Hence, the control task amounts to constructing the control evolution $U(t)$ to be of universal robustness, i.e.,

$$\int_0^T U^\dagger(t) V U(t) dt = 0, \quad (26)$$

for any V in the system's operator space. This reveals a core requirement for robust control: not only must the control implement the target gate at the final time $U(T) = \bar{U}$, but the entire evolution path $U(t)$ must be engineered to dynamically cancel out the noise perturbation throughout the duration of the operation.

Existing robust control strategies are often limited to mitigating noise along specific, pre-characterized directions. Techniques such as dynamical decoupling [60, 67, 68], composite pulses [69–72], and geometric evolution optimization [73–77] can suppress noise from several directions, but are generally difficult to generalize to arbitrary system dimensions and target gates. Conversely, while quantum error correction [89, 90] and feedback control [91, 92] can manage general noise, they incur substantial resource overhead, requiring either auxiliary qubits or adaptive measurements. An alternative approach employs multi-objective optimization to suppress multiple, coexisting noise channels concurrently [93, 94]. However, these numerical methods are often hampered by high computational complexity and a strong dependence on problem-specific parameters.

The recent work in Ref. [53] addresses universally robust control (URC) directly. The authors recognize that

the universally robust condition in Eq. (26) is equivalent to requiring the noise-free evolution $\{U(t)\}_{t=0}^T$ to form a unitary 1-design. To obtain such a unitary 1-design control, they employ numerical means. The total evolution is discretized into N segments of equal duration, and a control pulse is numerically optimized to render the resulting set of operators $\{U(t_k)\}_{k=0}^{N-1}$ a unitary 1-design. While effective for small systems, this approach faces computational bottlenecks for multi-qubit systems due to the exponential growth of the Hilbert space dimension. Furthermore, such numerical solutions often lack physical interpretability. These limitations highlight the need for analytical solutions to the URC problem.

We now employ the continuous unitary 1-designs constructed in the previous section to solve the URC problem. By definition, a continuous unitary 1-design $U(s)$ is a smooth path in $\mathbb{SU}(d)$ that satisfies

$$\int_{[0,1]} U^\dagger(s) V U(s) ds = \int_{\mathbb{SU}(d)} U^\dagger V U dU = \frac{I}{d} \text{Tr}(V) = 0,$$

for any traceless operator V , fulfilling the universally robust condition. Consequently, by inversely engineering the control fields from a predefined continuous unitary 1-design path, we obtain a direct and constructive method for synthesizing smooth URC fields. The following numerical simulations demonstrate the implementation and performance of this approach.

B. Analytic Control Solution

For our numerical analysis, we focus on the single-qubit system. We assume resonant controls that act along all three axes, described by the vector $\mathbf{u}(t) = (u_x(t), u_y(t), u_z(t))$ for $t \in [0, T]$, with a maximum Rabi frequency Ω such that $|\mathbf{u}(t)| \leq \Omega$. This control model is experimentally implementable. For instance, superconducting qubits utilize XY microwave drives and Z flux biases [95]. In the resonant frame, the control Hamiltonian is

$$H(t) = u_x(t) \frac{\sigma_x}{2} + u_y(t) \frac{\sigma_y}{2} + u_z(t) \frac{\sigma_z}{2}. \quad (27)$$

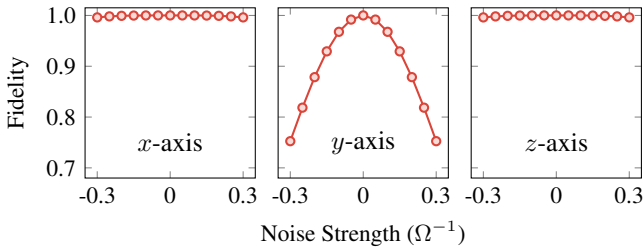


FIG. 5. A rectangular 2π rotation pulse about the y -axis generates a symmetric continuous unitary 1-design path capable of averaging out X and Z noise operators. This makes the pulse robust against noise with x - and z -components, but it remains highly susceptible to noise along the y -axis.

We employ the unitary 1-design path $U(\theta) = R_{\mathbf{n}_1}(\theta)R_{\mathbf{n}_2}(2\theta)$ from Eq. (7). It is important to note that this path is not realized by sequentially applying two gates. Rather, it represents a path parameterized by a path parameter $s \in [0, 1]$, which must be generated through continuously controlled evolution with respect to the physical time parameter t . We derive the corresponding URC field by solving the Schrödinger equation $U(\theta(t)) = -iH(t)U(\theta(t))$, yielding

$$\begin{aligned} H(t) &= i\dot{U}(\theta)U^\dagger(\theta) \\ &= \frac{d\theta}{dt} \left[\frac{1}{2}(\mathbf{n}_1 \cdot \boldsymbol{\sigma}) + R_{\mathbf{n}_1}(\theta)(\mathbf{n}_2 \cdot \boldsymbol{\sigma})R_{\mathbf{n}_1}^\dagger(\theta) \right] \\ &= \frac{d\theta}{dt} \left[\frac{1}{2}(\mathbf{n}_1 \cdot \boldsymbol{\sigma}) + [\cos \theta \mathbf{n}_2 + \sin \theta (\mathbf{n}_1 \times \mathbf{n}_2)] \cdot \boldsymbol{\sigma} \right], \end{aligned}$$

where we have used Pauli matrix identity $(\mathbf{n}_1 \cdot \boldsymbol{\sigma})(\mathbf{n}_2 \cdot \boldsymbol{\sigma}) = (\mathbf{n}_1 \cdot \mathbf{n}_2)I + i(\mathbf{n}_1 \times \mathbf{n}_2) \cdot \boldsymbol{\sigma}$. Comparing this with the Hamiltonian in Eq. (27), we identify the control field

$$\mathbf{u} = \frac{d\theta}{dt} [\mathbf{n}_1 + 2 \cos \theta \mathbf{n}_2 + 2 \sin \theta (\mathbf{n}_1 \times \mathbf{n}_2)]. \quad (28)$$

This control field must satisfy the power constraint $|\mathbf{u}(t)| \leq \Omega$, which amounts to the requirement $|d\theta/dt| \leq \Omega/\sqrt{5}$. In the case where θ is linearly parameterized as $\theta = 2\pi s$, the physical time t can be related to the path parameter s via $s = t\Omega/(2\pi\sqrt{5})$.

C. Numerical Simulations

1. Robust quantum gate

We first consider the implementation of a robust single-qubit identity gate, $\bar{U} = I$. In the presence of noise, a qubit's state becomes unstable. Applying active control to counteract these noise effects ensures the net evolution is the identity, thereby preserving quantum information. A robust identity gate is also useful in multi-qubit circuits for selectively decoupling and preserving the state of local qubits.

For noise restricted to one or two specific directions, we note that a simple square pulse is sufficient to achieve first-order decoupling. This is interpretable within the framework of symmetric unitary designs [96]. Consider, for instance, a noise operator $V = V_x \sigma_x/2 + V_z \sigma_z/2$ with nonzero x - and z -components. The discrete set $\{I, Y\}$ averages this noise to zero, since $IVI + YVY = 0$. This occurs because $\{I, Y\}$ constitutes a symmetric unitary 1-design for the Y -symmetric subgroup $\{U \in \mathbb{SU}(2) | [U, Y] = 0\}$, which is isomorphic to $\{R_y(\theta) | \theta \in \mathbb{R}\}$. Obviously, a continuous unitary 1-design path that connects the elements $\{I, Y\}$ is the subgroup $\{R_y(\theta)\}$ itself. The corresponding control field for this path is simply a constant square pulse effecting a 2π rotation about the y -axis.

However, if the noise has components along all three axes, a primitive square pulse about the y -axis becomes

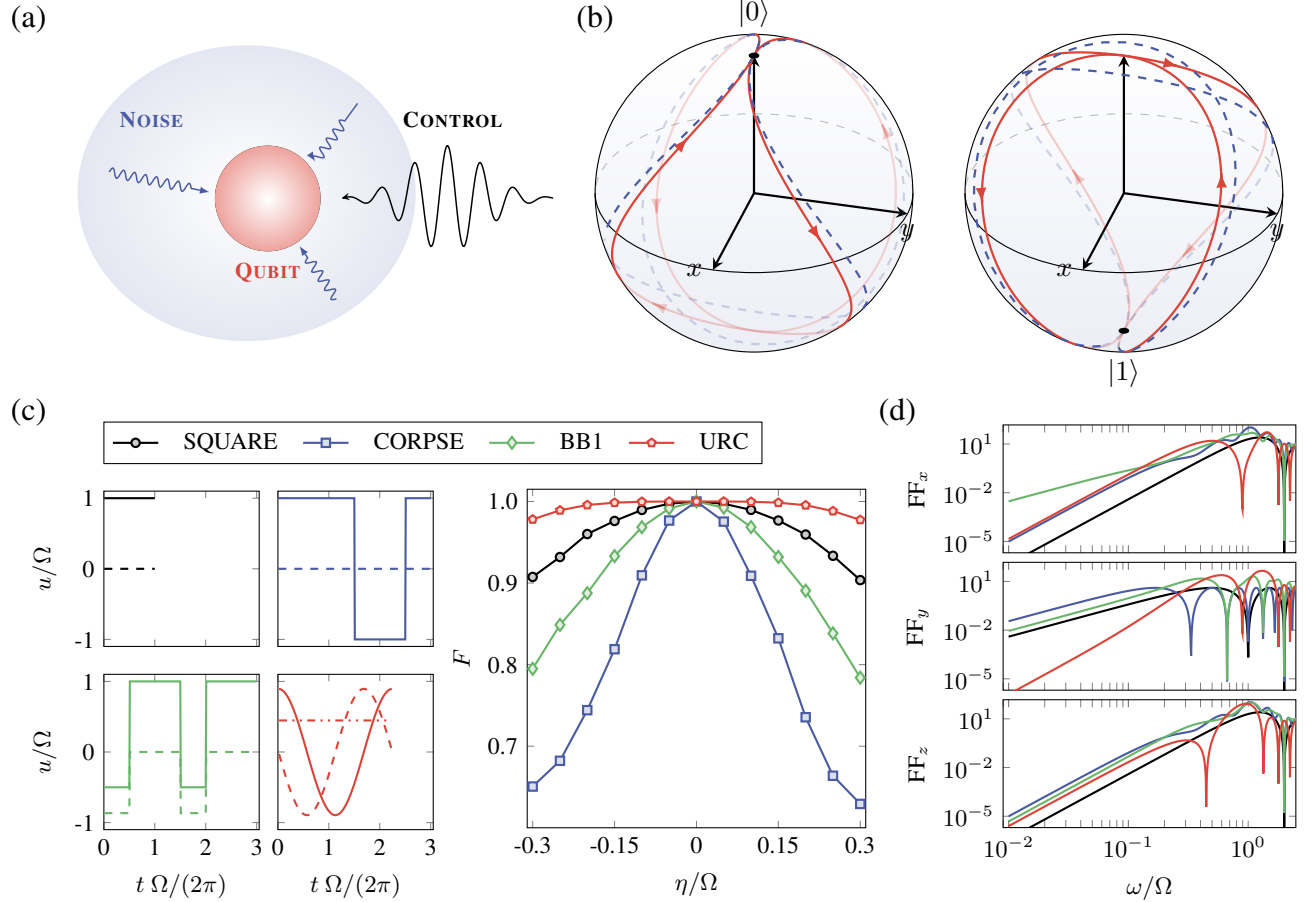


FIG. 6. Simulation results for implementing a single-qubit identity gate against an unknown noise environment using different control pulses. (a) Problem setup. A single qubit is subject to a generic noise perturbation with an unknown amplitude and orientation. The goal is to use active control to protect the qubit from this noise, thereby implementing an identity gate. (b) State evolution trajectories under URC pulse control, starting from the $|0\rangle$ state (left) or the $|1\rangle$ state (right). The solid curve represents the ideal evolution path (a state 1-design curve). The dashed curve shows the evolution when noise is present. Although the noisy evolution deviates from the ideal one, it automatically corrects the errors by the end of the evolution, forming a dynamically corrected gate. (c) Control waveforms and static noise robustness. The plots show the control waveforms for the different pulses. Dashed and solid lines represent the x - and y -components, respectively. For the URC pulse, a constant z -component is also present (dash-dotted line). All pulses are bounded by a maximum Rabi frequency Ω . The graph on the right compares the robustness of each pulse to static noise, showing the noise averaged gate fidelity F_N as a function of noise strength η . For each η , the noise-averaged fidelity F_N is computed from an average over 1000 random spatial orientations of the noise vector. (d) Robustness to time-varying noise. The filter functions FF_α ($\alpha = x, y, z$) for each pulse, quantifying their susceptibility to time-dependent noise along different spatial axes.

ineffective at suppressing its y -component, as illustrated in Fig. 6(a). In this more general case, finding a robust control is not as straightforward. Our continuous unitary design theory provides a solution, given by Eq. (28). Specifically, by choosing $\mathbf{n}_1 = (0, 0, 1)$, $\mathbf{n}_2 = (0, 1, 0)$, and $\theta = 2\pi s = \Omega t$, the URC pulse takes the form

$$\begin{cases} u_x(t) = -\frac{2\Omega}{\sqrt{5}} \sin\left(\frac{\Omega}{\sqrt{5}}t\right), \\ u_y(t) = \frac{2\Omega}{\sqrt{5}} \cos\left(\frac{\Omega}{\sqrt{5}}t\right), \\ u_z(t) = \frac{\Omega}{\sqrt{5}}, \end{cases} \quad (29)$$

with $t \in [0, 2\pi\sqrt{5}/\Omega]$. This pulse naturally implements a universally robust identity gate. For comparison, we also evaluate the widely used composite pulses CORPSE [97] and BB1 [98], which are designed to mitigate static detuning and amplitude noise, respectively. CORPSE consists of three elementary gates $R_{\phi_3}(\theta_3)R_{\phi_2}(\theta_2)R_{\phi_1}(\theta_1)$, where $\theta_1 = 3\pi, \theta_2 = 2\pi, \theta_3 = \pi$ and $\phi_1 = \phi_3 = \pi/2, \phi_2 = 3\pi/2$. BB1 consists of four elementary gates $R_{\phi'_4}(\theta'_4)R_{\phi'_3}(\theta'_3)R_{\phi'_2}(\theta'_2)R_{\phi'_1}(\theta'_1)$, where $\theta'_1 = \theta'_3 = \pi, \theta'_2 = \theta'_4 = 2\pi$ and $\phi'_1 = \phi'_3 = 7\pi/6, \phi'_2 = 5\pi/2, \phi'_4 = \pi/2$. The pulse waveforms for these sequences, along with the primitive square pulse, are shown in Fig. 6(c). We compare their performance by simulating the gate fidelity F

under static, randomly oriented three-dimensional noise with strength η ranging over $[0, 30\%\Omega]$, as also shown in Fig. 6(c). The results clearly show that both CORPSE and BB1 perform worse than the square pulse in this scenario. This is because they are designed to counteract a specific type of noise. For example, while CORPSE provides better robustness than SUQARE against detuning noise along z -axis, its average performance is lower when considering arbitrary noise orientations. In contrast, our URC pulse demonstrates superior, universal robustness, maintaining high gate fidelity across the entire range of tested noise. For visualization, in Fig. 6(b), we plotted the state evolution under URC pulse control. Applying a unitary 1-design to a quantum state generates a state 1-design. We observe that the state evolution trajectories are, as expected, evenly distributed on the Bloch sphere. When noise is present, the evolution deviates from its original path but eventually arrives at the target state, with errors being automatically corrected.

Furthermore, we investigate the robustness of the URC pulse against time-varying noise, where the noise amplitude fluctuates during the pulse execution. Previous research has shown that composite pulses can maintain robustness against time-dependent, non-Markovian noise at frequencies up to 10% of the Rabi frequency [99]. We therefore anticipate that our URC pulse possesses a similar capacity to mitigate low-frequency noise to a certain extent. To verify this, we employ the filter function (FF) formalism [100], which quantifies a control pulse's sensitivity to noise across different frequencies and thereby characterizes its impact on gate fidelity. The FF is typically defined as

$$\text{FF}_\alpha(\omega) = \sum_k \left| -i\omega \int_0^T R_{\alpha k}(t) e^{i\omega t} dt \right|^2, \quad (30)$$

where $R_{\alpha k}(t) = \text{Tr}[U^\dagger(t) \sigma_\alpha U(t) \sigma_k]/2$ and $\alpha, k = x, y, z$. Figure 6(d) compares the FFs along different directions for the primitive y -rotation, CORPSE, BB1, and URC pulses as shown in Fig. 6(c). We find that for low-frequency time-dependent noise along y -direction, the FF_y of the URC pulse is significantly smaller than that of all other pulses, confirming its superior robustness. Furthermore, we observe that the URC pulse exhibits filter functions of comparable magnitude along all three directions. In contrast, the other pulses only show markedly reduced FFs along one or two specific axes. This result underscores the URC pulse's unique ability to suppress time-dependent noise of arbitrary orientation.

2. Quantum memory

Next, we explore the application of continuous unitary 1-designs to qubit quantum memory. Conventionally, quantum memory is protected by dynamical decoupling, which preserves quantum coherence from environmental noise by repeatedly flipping the qubit so that

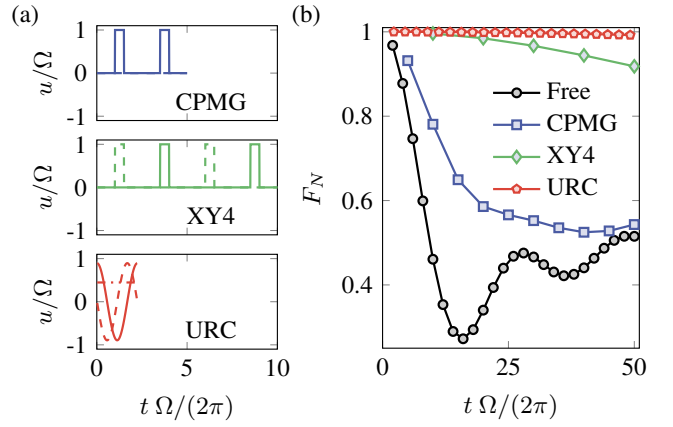


FIG. 7. Simulation results for quantum memory based on different DD sequences. (A) Control waveforms for each sequence, all subject to the power constraint $|\mathbf{u}| \leq \Omega$. (B) Decay of noise-averaged fidelity versus the number of sequence repetitions. The total memory time is identical for all sequences, requiring a different number of repetitions for each.

the qubit-environmental interaction is averaged out [101]. As demonstrated above, the URC pulse implements a robust identity gate, making it a promising candidate for quantum memory through repeated application. For comparison, we also evaluate standard dynamical decoupling sequences, including CPMG and XY4. The CPMG sequence [102], denoted as $f_\tau R_y(\pi) f_{2\tau} R_y(\pi) f_\tau$, where f_τ represents free evolution for a duration τ , is designed to suppress noise perpendicular to its pulse rotation axis. The XY4 sequence [103], taking the form $f_\tau R_y(\pi) f_{2\tau} R_x(\pi) f_{2\tau} R_y(\pi) f_{2\tau} R_x(\pi) f_\tau$, is engineered to mitigate noise along all three spatial directions. The explicit pulse waveforms for these sequences are shown in Fig. 7(a).

During each sequence, a noise perturbation with a strength up to 0.05Ω is applied along a random three-dimensional orientation. Each sequence (including free evolution periods) is repeated multiple times to generate a fidelity decay curve. Averaging over 100 noise realizations of different random directions and random strengths then gives the noise-averaged fidelity F_N , as shown in Fig. 7(b). As expected, we find that XY4 outperforms CPMG, since XY4 is designed to suppress noise along all three spatial directions, while CPMG only addresses two. The XY4 sequence is derived from the Pauli group $\{I, X, Y, Z\}$, which forms a unitary 1-design. Ideally, this design should enable the sequence to have universal decoupling ability. In practice, however, the finite duration of its π pulses, causes deviations from ideal instantaneous rotations, compromising its robustness against fully generic, three-dimensional noise. Remarkably, the URC sequence preserves the characteristics of a unitary 1-design throughout its continuous evolution. As a result, it maintains near-perfect coherence over the investigated time range, highlighting its signifi-

cant potential for realizing reliable quantum memory in universal noise environments.

VI. DISCUSSIONS AND OUTLOOK

Our work extends the scope of unitary design research from the discrete to the continuous domain. As an initial work, we have developed theoretical methods for constructing continuous unitary designs, provided explicit construction examples, and demonstrated their practical applications in quantum control.

We first dedicated considerable effort to constructing single-qubit unitary 1-design paths and elucidating their geometric and topological principles. Indeed, even for the single-qubit case, this task is highly non-trivial. Unitary designs basically aim to uniformly sample the unitary group $\text{SU}(2)$. A naive approach is to impose a coordinate system that treats the group manifold $\text{SU}(2)$ as a patch of \mathbb{R}^3 . However, many of such coordinate systems introduce metric distortions relative to the intrinsic geometry of the $\text{SU}(2)$. For example, random sampling of Euler angles (α, β, γ) in the XYZ decomposition $U = R_z(\alpha)R_y(\beta)R_z(\gamma)$ (up to a global phase) leads to significant redundant sampling. This method is particularly ill-suited for continuous paths, as it is prone to singularities [104] and gimbal lock [105]. The inefficiency comes from topological mismatch: the Euler angle representation has the topology of $\mathbb{S}^1 \times \mathbb{S}^1 \times \mathbb{S}^1$, which fails to capture the true topology of $\text{SU}(2)$. In contrast, the Hopf fibration correctly captures this topology. Consequently, Hopf coordinates naturally describe the intrinsic structure of $\text{SU}(2)$ and provide a tool for generating uniform distributions [106], explaining their essential role in constructing unitary design paths [58].

We also constructed open unitary 1-design paths by strategically modifying closed ones. The presented examples are approximate unitary designs when discretely sampled, but converge to exact designs with increasing sampling density. This limitation can be mitigated by a more sophisticated parameterization, for instance, by assigning a local weight to each segment and reparameterizing the path to make the sampling density inversely proportional to this weight, thereby ensuring adaptive and efficient coverage. These open unitary 1-design paths will find applications in dynamically corrected gates [30] and dynamical-decoupling-protected gates [107, 108], as they simultaneously implement a target quantum gate while averaging out noise-induced errors.

For higher-dimensional systems, we have presented two distinct methods for constructing unitary 1-design paths: one based on fiber bundle theory and the other on the Heisenberg-Weyl group. These methods yield paths of different lengths. The Heisenberg-Weyl approach draws upon a well-established framework in quantum information [109, 110], bearing a group-theoretic flavour. In contrast, the fiber bundle approach offers a complementary geometric perspective. This mathematical framework de-

scribes spaces that are locally simple yet may exhibit complex global topological twists. By revealing the underlying geometric structure of the unitary design paths, it brings powerful topological tools into play, thereby broadening the methodological landscape beyond traditional group-theoretic constructions.

Finally, we demonstrated the practical utility of our unitary 1-design paths by employing them to generate universally robust control pulses. These pulses achieve high-fidelity identity operations under arbitrary unknown static noise, as confirmed by numerical comparisons with conventional techniques. Furthermore, filter function analysis verifies their robustness against slowly varying noise. While the current sequences do not yet account for common experimental errors like Rabi inaccuracies [111, 112], this limitation can be directly addressed by incorporating time-symmetry between consecutive sequences [113, 114]. Moreover, our framework for constructing qudit unitary design paths can be directly applied to implement qudit dynamical decoupling [86, 115]. Given the persistent challenge of designing robust pulses in noisy environments, our work provides a valuable addition to the standard toolbox for robust quantum engineering.

Our study of continuous unitary designs paves the way for numerous promising research directions. Below, we outline several open questions that merit further investigation.

- (1) How to find optimal, or asymptotically optimal, continuous unitary 1-design paths? This problem, which mirrors the classical pursuit of optimal spherical designs [56, 58, 82], is of significant theoretical interest. On practical side, the shortest such path may lead to time-optimal control solutions in quantum control. While our work has presented several explicit unitary 1-design paths of varying lengths, we find that especially those constructed via the inductive procedure based on topological bundle theory (as described in Sec. IV B) exhibit a length that grows rapidly with the system dimension. We anticipate that shorter paths exist in abundance; identifying them warrants further exploration and may involve techniques from other mathematical theories, such as additive combinatorics [81, 116, 117].
- (2) This work focuses on continuous unitary 1-designs ($t = 1$) and their applications in quantum control. A natural next step is to construct continuous unitary designs for $t \geq 2$ and explore their potential applications. For $t = 2$, the most straightforward approach is to find a continuous path that passes through a discrete unitary 2-design set, such as the Clifford group, such that the path itself forms a continuous 2-design. In the single-qubit case, based on the correspondence between $\text{SU}(2)$ and \mathbb{S}^3 , a unitary 2-design can be derived from a spherical 4-design. The latter can be constructed using the

Hopf map technique described in Ref. [59], which involves placing a spherical 4-design on each fiber of the Hopf map associated with a 2-design curve on \mathbb{S}^2 . For higher-dimensional systems, the construction might become more challenging. Given a successful construction, it would be highly interesting to identify applications. Unitary 2-designs are crucial for many quantum information protocols, such as randomized benchmarking [31, 32], suggesting immediate practical utility.

(3) Continuous unitary designs can be integrated into Hamiltonian engineering as they enable controls over average Hamiltonians. There exist connections between unitary designs and decoupling sequences. A unitary 1-design, for example, serves as a universal decoupling group for its ability to average any traceless Hamiltonian to zero [86]. A more refined Hamiltonian decoupling can possibly be enabled by symmetric unitary designs [96]. Usually, decoupling sequences employ discrete, instantaneous π and $\pi/2$ pulses. We are thus to ask: can continuous pulse policies, derived from symmetric unitary designs, achieve the same decoupling goal? More broadly, analogous to the role of discrete pulse sequences in average Hamiltonian theory for engineering many-body spin dynamics [118], continuous unitary designs may provide a continuous framework for averaging out undesired interactions, thereby advancing the toolkit for Hamiltonian engineering.

In summary, this work establishes a foundation for several future research avenues. On the theoretical front, the further exploration of continuous unitary design construction promises to uncover new examples and stimulate the development of associated mathematical tools. For applications, these designs provide a practical tool for Hamiltonian engineering, directly advancing capabilities in quantum decoupling, sensing, and simulation.

VII. ACKNOWLEDGMENTS

This work is supported by the Innovation Program for Quantum Science and Technology (2024ZD0300400), the National Natural Science Foundation of China (grant no. 12441502, 12204230), and the Guangdong Provincial Quantum Science Strategic Initiative (GDZX2305006, GDZX2405002).

Appendix A: Continuous Spherical 2-design and Unitary 1-design for Qubit

Let V be a traceless Hermitian operator. In the Pauli basis, V admits the decomposition $V = \mathbf{v} \cdot \boldsymbol{\sigma}$, where

$\mathbf{v} \in \mathbb{R}^3$. Let U be a unitary matrix parameterized as

$$U = \begin{pmatrix} x_1 + ix_2 & x_3 + ix_4 \\ -x_3 + ix_4 & x_1 - ix_2 \end{pmatrix},$$

with $(x_1, x_2, x_3, x_4) \in \mathbb{S}^3 \subset \mathbb{R}^4$. This establishes the known identification of $\mathbb{SU}(2) \cong \mathbb{S}^3$. The conjugation $W = UVU'$ preserves both the Hermitian and traceless properties of V , so it can be expressed as $W = \mathbf{w} \cdot \boldsymbol{\sigma}$ for some $\mathbf{w} \in \mathbb{R}^3$. A direct computation shows that each component w_k is a homogeneous quadratic form in x , specifically, $w_k = x A_k x^T$, where the symmetric matrices A_k are given by

$$A_1 = \begin{pmatrix} v_1 & v_2 & -v_3 & 0 \\ v_2 & -v_1 & 0 & v_3 \\ -v_3 & 0 & -v_1 & v_2 \\ 0 & v_3 & v_2 & v_1 \end{pmatrix},$$

$$A_2 = \begin{pmatrix} v_2 & -v_1 & 0 & v_3 \\ -v_1 & -v_2 & v_3 & 0 \\ 0 & v_3 & -v_2 & v_1 \\ v_3 & 0 & v_1 & -v_2 \end{pmatrix},$$

$$A_3 = \begin{pmatrix} v_3 & 0 & v_1 & -v_2 \\ 0 & v_3 & v_2 & v_1 \\ v_1 & v_2 & -v_3 & 0 \\ -v_2 & v_1 & 0 & -v_3 \end{pmatrix}.$$

On the 3-sphere \mathbb{S}^3 , the following integration identity holds for the coordinate functions: $\int_{\mathbb{S}^3} x_k x_j d\mu = \delta_{kj}/4$. Suppose γ is a spherical 2-design curve in \mathbb{S}^3 , meaning that for any polynomial f of degree at most 2, there is $\frac{1}{\ell(\gamma)} \int_{\gamma} f ds = \int_{\mathbb{S}^3} f d\mu$, so

$$\frac{1}{\ell(\gamma)} \int_{\gamma} w_k ds = \int_{\mathbb{S}^3} w_k d\mu = \frac{1}{4} \text{Tr } A_k = 0.$$

Now, let U_{γ} be the unitary path in $\mathbb{SU}(2)$ corresponding to γ , we thence have

$$\frac{1}{\ell(\gamma)} \int_{U_{\gamma}} UVU' dU = \frac{1}{\ell(\gamma)} \int_{\gamma} \mathbf{w} \cdot \boldsymbol{\sigma} ds = 0,$$

which holds for all traceless Hermitian V . This implies that U_{γ} is a unitary 1-design path.

Appendix B: Stereographic Projection

Stereographic projection provides a powerful method for visualizing the geometry of the 3-sphere \mathbb{S}^3 by mapping it onto \mathbb{R}^3 . We employ this technique to visualize the design curves on \mathbb{S}^3 .

Consider the Hopf fibration $\mathbb{S}^1 \hookrightarrow \mathbb{S}^3 \xrightarrow{\pi} \mathbb{S}^2$, where π is Hopf map. Let C denote the preimage of the great circle $(0, \cos \theta, \sin \theta)$ in the base \mathbb{S}^2 . This preimage is a circle of circles (fibers), namely a torus, named the Clifford torus, having the explicit formula

$$C(\theta, \phi) = \frac{1}{\sqrt{2}}(\cos \theta, \sin \theta, \cos \phi, \sin \phi),$$

where $\theta, \phi \in [0, 2\pi]$. To visualize this geometric object embedded in \mathbb{S}^3 , we employ the stereographic projection $f : \mathbb{S}^3 \setminus (0, 0, 0, -1) \rightarrow \mathbb{R}^3$ from the south pole $(0, 0, 0, -1)$ to the equatorial plane $x_4 = 0$, defined by

$$f(x_1, x_2, x_3, x_4) = \frac{1}{1+x_4}(x_1, x_2, x_3).$$

This conformal mapping preserves angles and local shapes, establishing a homeomorphism between the punctured sphere and the plane. Under this projection, the Clifford torus transforms to

$$f(C) = \frac{1}{\sqrt{2} + \sin \phi}(\cos \theta, \sin \theta, \cos \phi),$$

revealing its structure in three dimensional space. The spherical design curves ξ in Eq. (9) and γ in Eq. (10)

both reside on this torus, projecting to

$$f(\xi) = \frac{1}{\sqrt{2} + \sin 2\theta}(\cos \theta, \sin \theta, \cos 2\theta)$$

$$f(\gamma) = \frac{1}{\sqrt{2} - \sin 3\theta}(\cos \theta, \sin \theta, \cos 3\theta)$$

The design curves ξ' in Eq. (12) and γ' in Eq. (13) are obtained from ξ and γ , respectively, through application of the same four-dimensional rotation R . These rotated curves reside on a different torus in \mathbb{S}^3 , specifically the Clifford torus transformed by the rotation

$$R(C) = (\cos \theta \cos \phi, \cos \theta \sin \phi, \sin \theta \cos \phi, \sin \theta \sin \phi),$$

where $\theta, \phi \in [0, 2\pi]$. By applying a corresponding rotation to both the center of projection and the projection plane, we maintain the same visualization characteristics as in the unrotated case.

[1] M. A. Nielsen and I. L. Chuang, *Quantum Computation and Quantum Information* (Cambridge University Press, 2000).

[2] J. Emerson, Y. S. Weinstein, M. Saraceno, S. Lloyd, and D. G. Cory, Pseudo-random unitary operators for quantum information processing, *Science* **302**, 2098 (2003).

[3] D. Gross, K. Audenaert, and J. Eisert, Evenly distributed unitaries: On the structure of unitary designs, *J. Math. Phys.* **48**, 052104 (2007).

[4] C. Dankert, R. Cleve, J. Emerson, and E. Livine, Exact and approximate unitary 2-designs and their application to fidelity estimation, *Phys. Rev. A* **80**, 012304 (2009).

[5] P. S. Turner and D. Markham, Derandomizing quantum circuits with measurement-based unitary designs, *Phys. Rev. Lett.* **116**, 200501 (2016).

[6] A. W. Harrow and R. A. Low, Random quantum circuits are approximate 2-designs, *Commun. Math. Phys.* **291**, 257 (2009).

[7] W. G. Brown and L. Viola, Convergence rates for arbitrary statistical moments of random quantum circuits, *Phys. Rev. Lett.* **104**, 250501 (2010).

[8] F. G. S. L. Brandão, A. W. Harrow, and M. Horodecki, Local random quantum circuits are approximate polynomial-designs, *Commun. Math. Phys.* **346**, 397 (2016).

[9] F. G. S. L. Brandão, A. W. Harrow, and M. Horodecki, Efficient quantum pseudorandomness, *Phys. Rev. Lett.* **116**, 170502 (2016).

[10] Y. Mitsuhashi, R. Suzuki, T. Soejima, and N. Yoshioka, Unitary designs of symmetric local random circuits, *Phys. Rev. Lett.* **134**, 180404 (2025).

[11] A. W. Harrow and S. Mehraban, Approximate unitary t-designs by short random quantum circuits using nearest-neighbor and long-range gates, *Commun. Math. Phys.* **401**, 1531 (2023).

[12] Z. Li, H. Zheng, J. Liu, L. Jiang, and Z.-W. Liu, Designs from local random quantum circuits with $SU(d)$ symmetry, *PRX Quantum* **5**, 040349 (2024).

[13] D. Belkin, J. Allen, S. Ghosh, C. Kang, S. Lin, J. Sud, F. T. Chong, B. Fefferman, and B. K. Clark, Approximate t -designs in generic circuit architectures, *PRX Quantum* **5**, 040344 (2024).

[14] S. N. Hearth, M. O. Flynn, A. Chandran, and C. R. Laumann, Unitary k -designs from random number-conserving quantum circuits, *Phys. Rev. X* **15**, 021022 (2025).

[15] Y. Nakata, C. Hirche, M. Koashi, and A. Winter, Efficient quantum pseudorandomness with nearly time-independent hamiltonian dynamics, *Phys. Rev. X* **7**, 021006 (2017).

[16] J. Li, Z. Luo, T. Xin, H. Wang, D. Kribs, D. Lu, B. Zeng, and R. Laflamme, Experimental implementation of efficient quantum pseudorandomness on a 12-spin system, *Phys. Rev. Lett.* **123**, 030502 (2019).

[17] R. Mezher, J. Ghalbouni, J. Dgheim, and D. Markham, Efficient quantum pseudorandomness with simple graph states, *Phys. Rev. A* **97**, 022333 (2018).

[18] L. Banchi, D. Burgarth, and M. J. Kastoryano, Driven quantum dynamics: Will it blend?, *Phys. Rev. X* **7**, 041015 (2017).

[19] J. Haferkamp, F. Montealegre-Mora, M. Heinrich, J. Eisert, D. Gross, and I. Roth, Efficient unitary designs with a system-size independent number of non-clifford gates, *Commun. Math. Phys.* **397**, 995 (2023).

[20] D. A. Roberts and B. Yoshida, Chaos and complexity by design, *J. High Energ. Phys.* **2017**, 121.

[21] J. Choi, A. L. Shaw, I. S. Madjarov, X. Xie, R. Finkelstein, J. P. Covey, J. S. Cotler, D. K. Mark, H.-Y. Huang, A. Kale, H. Pichler, F. G. S. L. Brandão, S. Choi, and M. Endres, Preparing random states and benchmarking with many-body quantum chaos, *Nature* **613**, 468 (2023).

[22] W.-K. Mok, T. Haug, A. L. Shaw, M. Endres, and J. Preskill, Optimal conversion from classical to quantum randomness via quantum chaos, *Phys. Rev. Lett.* **134**, 180403 (2025).

[23] M. Fava, J. Kurchan, and S. Pappalardi, Designs via free probability, *Phys. Rev. X* **15**, 011031 (2025).

[24] Z.-W. Liu, S. Lloyd, E. Zhu, and H. Zhu, Entanglement, quantum randomness, and complexity beyond scrambling, *J. High Energy Phys.* **2018** (7), 1.

[25] A. Nahum, J. Ruhman, S. Vijay, and J. Haah, Quantum entanglement growth under random unitary dynamics, *Phys. Rev. X* **7**, 031016 (2017).

[26] Z.-W. Liu, S. Lloyd, E. Y. Zhu, and H. Zhu, Generalized entanglement entropies of quantum designs, *Phys. Rev. Lett.* **120**, 130502 (2018).

[27] J. Haferkamp, P. Faist, N. B. Kothakonda, J. Eisert, and N. Yunger Halpern, Linear growth of quantum circuit complexity, *Nat. Phys.* **18**, 528 (2022).

[28] F. G. Brandão, W. Chemissany, N. Hunter-Jones, R. Kueng, and J. Preskill, Models of quantum complexity growth, *PRX Quantum* **2**, 030316 (2021).

[29] L. Viola, E. Knill, and S. Lloyd, Dynamical decoupling of open quantum systems, *Phys. Rev. Lett.* **82**, 2417 (1999).

[30] K. Khodjasteh and L. Viola, Dynamically error-corrected gates for universal quantum computation, *Phys. Rev. Lett.* **102**, 080501 (2009).

[31] J. Emerson, M. Silva, O. Moussa, C. Ryan, M. Laforest, J. Baugh, D. G. Cory, and R. Laflamme, Symmetrized characterization of noisy quantum processes, *Science* **317**, 1893 (2007).

[32] C. Dankert, R. Cleve, J. Emerson, and E. Livine, Exact and approximate unitary 2-designs and their application to fidelity estimation, *Phys. Rev. A* **80**, 012304 (2009).

[33] E. Magesan, J. M. Gambetta, and J. Emerson, Scalable and robust randomized benchmarking of quantum processes, *Phys. Rev. Lett.* **106**, 180504 (2011).

[34] I. Roth, R. Kueng, S. Kimmel, Y.-K. Liu, D. Gross, J. Eisert, and M. Kliesch, Recovering quantum gates from few average gate fidelities, *Phys. Rev. Lett.* **121**, 170502 (2018).

[35] A. Hashim, L. B. Nguyen, N. Goss, B. Marinelli, R. K. Naik, T. Chistolini, J. Hines, J. Marceaux, Y. Kim, P. Gokhale, T. Tomesh, S. Chen, L. Jiang, S. Ferencin, K. Rudinger, T. Proctor, K. C. Young, I. Siddiqi, and R. Blume-Kohout, Practical introduction to benchmarking and characterization of quantum computers, *PRX Quantum* **6**, 030202 (2025).

[36] Y. Nakata, D. Zhao, T. Okuda, E. Bannai, Y. Suzuki, S. Tamiya, K. Heya, Z. Yan, K. Zuo, S. Tamate, Y. Tabuchi, and Y. Nakamura, Quantum circuits for exact unitary t -designs and applications to higher-order randomized benchmarking, *PRX Quantum* **2**, 030339 (2021).

[37] P. Hayden, D. Leung, P. W. Shor, and A. Winter, Randomizing quantum states: Constructions and applications, *Commun. Math. Phys.* **250**, 371 (2004).

[38] C. Lancien and C. Majenz, Weak approximate unitary designs and applications to quantum encryption, *Quantum* **4**, 313 (2020).

[39] M. Oszmaniec, R. Augusiak, C. Gogolin, J. Kołodyński, A. Acín, and M. Lewenstein, Random bosonic states for robust quantum metrology, *Phys. Rev. X* **6**, 041044 (2016).

[40] Z. Cheng, E. Huang, V. Khemani, M. J. Gullans, and M. Ippoliti, Emergent unitary designs for encoded qubits from coherent errors and syndrome measurements, *PRX Quantum* **6**, 030333 (2025).

[41] J. R. McClean, S. Boixo, V. N. Smelyanskiy, R. Babbush, and H. Neven, Barren plateaus in quantum neural network training landscapes, *Nat. Commun.* **9**, 4812 (2018).

[42] K. Kaneko, E. Iyoda, and T. Sagawa, Characterizing complexity of many-body quantum dynamics by higher-order eigenstate thermalization, *Phys. Rev. A* **101**, 042126 (2020).

[43] P. Figueroa-Romero, F. A. Pollock, and K. Modi, Markovianization with approximate unitary designs, *Commun. Phys.* **4**, 127 (2021).

[44] S. Pilatowsky-Cameo, I. Marvian, S. Choi, and W. W. Ho, Hilbert-space ergodicity in driven quantum systems: Obstructions and designs, *Phys. Rev. X* **14**, 041059 (2024).

[45] T. Schuster, J. Haferkamp, and H.-Y. Huang, Random unitaries in extremely low depth, *Science* **389**, 92 (2025).

[46] Y. Nakata, Y. Takeuchi, M. Kliesch, and A. Darmawan, Computational complexity of unitary and state design properties, *PRX Quantum* **6**, 030345 (2025).

[47] G. Lami, T. Haug, and J. De Nardis, Quantum state designs with clifford-enhanced matrix product states, *PRX Quantum* **6**, 010345 (2025).

[48] J. Conrad, J. T. Iosue, A. G. Burchards, and V. V. Albert, Continuous-variable designs and design-based shadow tomography from random lattices, *Phys. Rev. Lett.* **135**, 060802 (2025).

[49] J. Haferkamp, D. Hangleiter, A. Bouland, B. Fefferman, J. Eisert, and J. Bermejo-Vega, Closing gaps of a quantum advantage with short-time hamiltonian dynamics, *Phys. Rev. Lett.* **125**, 250501 (2020).

[50] H. Zhu, Permutation symmetry determines the discrete wigner function, *Phys. Rev. Lett.* **116**, 040501 (2016).

[51] A. Ketterer, N. Wyderka, and O. Gühne, Entanglement characterization using quantum designs, *Quantum* **4**, 325 (2020).

[52] W. Gong, D. Yuan, W. Li, and D.-L. Deng, Enhancing quantum adversarial robustness by randomized encodings, *Phys. Rev. Res.* **6**, 023020 (2024).

[53] P. M. Poggi, G. De Chiara, S. Campbell, and A. Kiely, Universally robust quantum control, *Phys. Rev. Lett.* **132**, 193801 (2024).

[54] M. Adam, *Applications of unitary k -designs in quantum information processing*, Ph.D. thesis, Masarykova univerzita, Fakulta informatiky (2013).

[55] P. Delsarte, J. M. Goethals, and J. J. Seidel, Spherical codes and designs, *Geom. Dedicata* **6**, 363 (1977).

[56] M. Ehler and K. Gröchenig, t -design curves and mobile sampling on the sphere, *Forum Math. Sigma* **11**, e105, 1 (2023), 2020 Mathematics Subject Classification: Primary 41A55; Secondary 41A63, 94A12, 26B15.

[57] M. Ehler, K. Gröchenig, and C. Karner, Geodesic cycles on the sphere: t -designs and marcinkiewicz-zygmund inequalities (2025), arXiv:2501.06120v1.

[58] A. Lindblad, Asymptotically Optimal t -design Curves on S^3 (2025), arXiv:2408.04044v2.

[59] A. Lindblad, Designs related through projective and hopf maps (2025), arXiv:2310.12091v3.

[60] L. Viola and E. Knill, Robust dynamical decoupling of quantum systems with bounded controls, *Phys. Rev. Lett.* **90**, 037901 (2003).

[61] D. Husemöller, *Fibre Bundles* (Springer, 1993).

[62] T. Frankel, *The Geometry of Physics: An Introduction* (Cambridge University Press, 2011).

[63] R. Harper, S. T. Flammia, and J. J. Wallman, Efficient

learning of quantum noise, *Nat. Phys.* **16**, 1184 (2020).

[64] M. Reagor, C. B. Osborn, N. Tezak, A. Staley, G. Prawiroatmodjo, M. Scheer, N. Alidoust, E. A. Sete, N. Didier, M. P. da Silva, *et al.*, Demonstration of universal parametric entangling gates on a multi-qubit lattice, *Sci. Adv.* **4**, eaao3603 (2018).

[65] V. Schäfer, C. Ballance, K. Thirumalai, L. Stephen-son, T. Ballance, A. Steane, and D. Lucas, Fast quantum logic gates with trapped-ion qubits, *Nature* **555**, 75 (2018).

[66] C. A. Weidner, E. A. Reed, J. Monroe, B. Sheller, S. O’Neil, E. Maas, E. A. Jonckheere, F. C. Langbein, and S. Schirmer, Robust quantum control in closed and open systems: Theory and practice, *Automatica* **172**, 111987 (2025).

[67] L. Viola, E. Knill, and S. Lloyd, Dynamical decoupling of open quantum systems, *Phys. Rev. Lett.* **82**, 2417 (1999).

[68] X. Yang, Y. Ge, B. Zhang, and J. Li, Robust dynamical decoupling for the manipulation of a spin network via a single spin, *Phys. Rev. Appl.* **18**, 054075 (2022).

[69] M. H. Levitt, Composite pulses, *Prog. Nucl. Magn. Reson. Spectrosc.* **18**, 61 (1986).

[70] H. K. Cummins, G. Llewellyn, and J. A. Jones, Tackling systematic errors in quantum logic gates with composite rotations, *Phys. Rev. A* **67**, 042308 (2003).

[71] K. R. Brown, A. W. Harrow, and I. L. Chuang, Arbitrarily accurate composite pulse sequences, *Phys. Rev. A* **70**, 052318 (2004).

[72] M. Bando, T. Ichikawa, Y. Kondo, and M. Nakahara, Concatenated Composite Pulses Compensating Simultaneous Systematic Errors, *J. Phys. Soc. Jpn.* **82**, 014004 (2013).

[73] D. Daems, A. Ruschhaupt, D. Sugny, and S. Guérin, Robust Quantum Control by a Single-Shot Shaped Pulse, *Phys. Rev. Lett.* **111**, 050404 (2013).

[74] G. Dridi, K. Liu, and S. Guérin, Optimal Robust Quantum Control by Inverse Geometric Optimization, *Phys. Rev. Lett.* **125**, 250403 (2020).

[75] J. Zeng, C. H. Yang, A. S. Dzurak, and E. Barnes, Geometric formalism for constructing arbitrary single-qubit dynamically corrected gates, *Phys. Rev. A* **99**, 052321 (2019).

[76] D. Buterakos, S. Das Sarma, and E. Barnes, Geometrical formalism for dynamically corrected gates in multi-qubit systems, *PRX Quantum* **2**, 010341 (2021).

[77] X. Yang, Y. Li, R. Liu, X. Nie, T. Xin, D. Lu, and J. Li, Quantum control for time-dependent noise by inverse geometric optimization, *Sci. China-Phys. Mech. Astron.* **67**, 290312 (2024).

[78] T. Chen, J.-Q. Hu, C. Zhang, and Z.-Y. Xue, Universal robust geometric quantum control via geometric trajectory correction, *Phys. Rev. Appl.* **22**, 014060 (2024).

[79] L. Ding, J. Fan, and X. Qiu, Universally robust control of open quantum systems (2025), arXiv:2508.07379.

[80] H. Zhu, Multiqubit clifford groups are unitary 3-designs, *Phys. Rev. A* **96**, 062336 (2017).

[81] E. Bannai and E. Bannai, A survey on spherical designs and algebraic combinatorics on spheres, *Eur. J. Comb.* **30**, 1392 (2009).

[82] A. Bondarenko, D. Radchenko, and M. Viazovska, Optimal asymptotic bounds for spherical designs, *Ann. Math.* **178**, 443 (2013).

[83] H. Hopf, Über die abbildungen der dreidimensionalen sphäre auf die kugelfläche, *Math. Ann.* **104**, 637 (1931).

[84] G. Khanna, S. Mukhopadhyay, R. Simon, and N. Mukunda, Geometric phases for $su(3)$ representations and three level quantum systems, *Annals of Physics* **253**, 55 (1997).

[85] R. A. Bertlmann and P. Krammer, Bloch vectors for qudits, *J. Phys. A: Math. Theor.* **41**, 235303 (2008).

[86] V. Tripathi, N. Goss, A. Vezvae, L. B. Nguyen, I. Siddiqi, and D. A. Lidar, Qudit dynamical decoupling on a superconducting quantum processor, *Phys. Rev. Lett.* **134**, 050601 (2025).

[87] M. A. Yurtalan, J. Shi, M. Kononenko, A. Lupascu, and S. Ashhab, Implementation of a walsh-hadamard gate in a superconducting qutrit, *Phys. Rev. Lett.* **125**, 180504 (2020).

[88] F. J. Dyson, The radiation theories of tomonaga, schwinger, and feynman, *Phys. Rev.* **75**, 486 (1949).

[89] E. Knill, R. Laflamme, and L. Viola, Theory of quantum error correction for general noise, *Phys. Rev. Lett.* **84**, 2525 (2000).

[90] S. J. Devitt, W. J. Munro, and K. Nemoto, Quantum error correction for beginners, *Rep. Prog. Phys.* **76**, 076001 (2013).

[91] C. Brif, R. Chakrabarti, and H. Rabitz, Control of quantum phenomena: past, present and future, *New J. Phys.* **12**, 075008 (2010).

[92] J. Zhang, Y.-x. Liu, R.-B. Wu, K. Jacobs, and F. Nori, Quantum feedback: Theory, experiments, and applications, *Phys. Rep.* **679**, 1 (2017).

[93] H. Haas, D. Puzzuoli, F. Zhang, and D. G. Cory, Linear growth of quantum circuit complexity, *New J. Phys.* **21**, 103011 (2019).

[94] B. Shao, X. Yang, R. Liu, Y. Zhai, D. Lu, T. Xin, and J. Li, Multiple classical noise mitigation by multiobjective robust quantum optimal control, *Phys. Rev. Appl.* **21**, 034042 (2024).

[95] P. Krantz, M. Kjaergaard, F. Yan, T. P. Orlando, S. Gustavsson, and W. D. Oliver, A quantum engineer’s guide to superconducting qubits, *Appl. Phys. Rev.* **6**, 021318 (2019).

[96] Y. Mitsuhashi and N. Yoshioka, Clifford group and unitary designs under symmetry, *PRX Quantum* **4**, 040331 (2023).

[97] H. K. Cummins, G. Llewellyn, and J. A. Jones, Tackling systematic errors in quantum logic gates with composite rotations, *Phys. Rev. A* **67**, 042308 (2003).

[98] K. R. Brown, A. W. Harrow, and I. L. Chuang, Arbitrarily accurate composite pulse sequences, *Phys. Rev. A* **70**, 052318 (2004).

[99] C. Kabtyayev, T. J. Green, K. Khodjasteh, M. J. Biercuk, L. Viola, and K. R. Brown, Robustness of composite pulses to time-dependent control noise, *Phys. Rev. A* **90**, 012316 (2014).

[100] T. J. Green, J. Sastrawan, H. Uys, and M. J. Biercuk, Arbitrary quantum control of qubits in the presence of universal noise, *New J. Phys.* **15**, 95004 (2013).

[101] D. Suter and G. A. Álvarez, Colloquium: Protecting quantum information against environmental noise, *Rev. Mod. Phys.* **88**, 041001 (2016).

[102] S. Meiboom and D. Gill, Modified spinecho method for measuring nuclear relaxation times, *Rev. Sci. Instrum.* **29**, 688 (1958).

[103] T. Gullion, D. B. Baker, and M. S. Conradi, New, compensated Carr-Purcell sequences, *J. Magn. Reson.* **89**,

479 (1990).

[104] J. Stuelpnagel, On the parametrization of the three-dimensional rotation group, *SIAM review* **6**, 422 (1964).

[105] K. Shoemake, Animating rotation with quaternion curves, in *Proceedings of the 12th annual conference on Computer graphics and interactive techniques* (1985) pp. 245–254.

[106] A. Yershova, S. Jain, S. M. LaValle, and J. C. Mitchell, Generating uniform incremental grids on $so(3)$ using the hopf fibration, *Int. J. Robot. Res.* **29**, 801 (2010).

[107] J. R. West, D. A. Lidar, B. H. Fong, and M. F. Gyure, High fidelity quantum gates via dynamical decoupling, *Phys. Rev. Lett.* **105**, 230503 (2010).

[108] J. Zhang, A. M. Souza, F. D. Brandao, and D. Suter, Protected quantum computing: Interleaving gate operations with dynamical decoupling sequences, *Phys. Rev. Lett.* **112**, 050502 (2014).

[109] A. Vourdas, Quantum systems with finite hilbert space, *Rep. Prog. Phys.* **67**, 267 (2004).

[110] Y. Wang, Z. Hu, B. C. Sanders, and S. Kais, Qudits and high-dimensional quantum computing, *Front. Phys.* **8**, 589504 (2020).

[111] G. A. Álvarez, A. Ajoy, X. Peng, and D. Suter, Performance comparison of dynamical decoupling sequences for a qubit in a rapidly fluctuating spin bath, *Phys. Rev. A* **82**, 042306 (2010).

[112] G. T. Genov, D. Schraft, N. V. Vitanov, and T. Halfmann, Arbitrarily accurate pulse sequences for robust dynamical decoupling, *Phys. Rev. Lett.* **118**, 133202 (2017).

[113] L. M. K. Vandersypen and I. L. Chuang, Nmr techniques for quantum control and computation, *Rev. Mod. Phys.* **76**, 1037 (2005).

[114] A. Brinkmann, Introduction to average Hamiltonian theory. I. Basics, *Concepts Magn. Reson. Part A* **45**, e21414 (2016).

[115] R. d. J. Napolitano, F. F. Fanchini, A. H. da Silva, and B. Bellomo, Protecting operations on qudits from noise by continuous dynamical decoupling, *Phys. Rev. Res.* **3**, 013235 (2021).

[116] B. Bajnok, *Additive Combinatorics: A Menu of Research Problems* (Chapman & Hall, 2018).

[117] B. Bajnok, Additive combinatorics in groups and geometric combinatorics on spheres, in *Combinatorics, Graph Theory and Computing*, edited by S. Heuss, R. Low, and J. C. Wierman (Springer Proceedings in Mathematics & Statistics 462, 2024) pp. 1–15.

[118] J. Choi, H. Zhou, H. S. Knowles, R. Landig, S. Choi, and M. D. Lukin, Robust dynamic hamiltonian engineering of many-body spin systems, *Phys. Rev. X* **10**, 031002 (2020).